Acta Geotechnica (2026) 21:1923–1949
https://doi.org/10.1007/s11440-025-02913-3

RESEARCH PAPER

An experimental and numerical study on the influence of inherent and induced anisotropy of a fine-grained soil

Merita Tafili[1] · **Sabine Gehring**[2] · **Lukas Knittel**[3] · **Torsten Wichtmann**[1] · **Hans H. Stutz**[2]

Received: 2 July 2025 / Accepted: 5 December 2025 / Published online: 22 February 2026

Abstract

This study investigates the inherent and induced anisotropy of reconstituted kaolin samples through a series of triaxial tests in both extension and compression under various preloading conditions. Triaxial specimens were extracted from pre-consolidated cylinders either in the vertical or horizontal direction to assess anisotropic behaviour. Additionally, different preshearing steps were applied to examine their influence on inherent anisotropy. Numerical simulations using the modified Cam Clay model and the anisotropic visco-hypoplastic model failed to capture the effects of inherent anisotropy. To address this limitation, the latter model was extended by incorporating a cross-isotropic elastic stiffness formulation. By increasing the number of parameters and model complexity, this study systematically evaluates which parameters and mathematical formulations are essential for accurately describing the stiffness anisotropy of reconstituted fine-grained soils.

Keywords (inherent) anisotropy · fine-grained soil · preshearing · anisotropic visco-hypoplasticity · constitutive modelling

1 Introduction

This study investigates the influence of inherent and induced anisotropy on the behaviour of fine-grained soil through a novel combined experimental and numerical approach. Anisotropy, the directional dependence of material properties, plays a crucial role in the mechanical response of soils. Inherent anisotropy is commonly defined to arise from soil formation processes such as sedimentation and deposition, influenced by factors like particle orientation, layering, and fabric. Several experimental studies on soft soils have shown that inherent anisotropy develops during sedimentation and one-dimensional consolidation due to the preferential alignment of particles or aggregates, leading to a mechanical response dependent on the loading direction [9, 16, 20, 33, 43, 48, 70, 72, 74]. However, some studies on reconstituted clay samples report little to no pronounced inherent anisotropy [11, 67, 13, 21, 57]. Among one of its manifestations is the anisotropy of the elastic tangent stiffness, which is a complex subject and not easily to be quantified (e.g. [16, 17, 36, 55, 75, 78]). Its impact in boundary value problems should not be ignored as pointed out through simulations of shallow foundations [34, 65], slope stability problems [58], tunnel excavations [1, 19] and excavations of construction pits [6, 18, 23, 40].

Induced anisotropy, on the other hand, is developed as a result of external forces or boundary conditions acting on the soil. These could include compaction, consolidation, shearing, or stress changes due to previous loading [20, 28, 32]. Both types of anisotropy interact and influence the mechanical behaviour of these soils by affecting their strength, shear behaviour, consolidation, settlement, permeability, and deformation characteristics [15, 28, 37]. The interaction can either reinforce or diminish the effects of anisotropy, depending on the alignment or misalignment of the anisotropic structures under different loading and stress

---

✉ Merita Tafili
merita.tafili@ruhr-uni-bochum.de

[1] Chair of Soil Mechanics, Foundation Engineering and Environmental Geotechnics, Ruhr-University Bochum, Bochum, Germany

[2] Institute of Soil Mechanics and Rock Mechanics, Karlsruhe Institute of Technology, Karlsruhe, Germany

[3] Chair of Geotechnics, Institute of Civil Engineering , University of Applied Sciences and Arts Northwestern Switzerland, Muttenz, Basel-Landschaft, Switzerland

conditions [2, 30, 68]. Although inherent anisotropy arises from the preferential orientation of particles within the soil and can, in a broader sense, be considered a form of induced anisotropy, the distinction between inherent and induced anisotropy is commonly made in the literature. While this separation may be somewhat artificial, it is adopted in this study for consistency. If the induced anisotropy aligns with the inherent anisotropy, it can accelerate consolidation and settlement along those directions. Conversely, if the induced anisotropy opposes the inherent anisotropy, it can impede consolidation and settlement. A quantification of these types of anisotropy is important for the prediction of settlements and bearing capacity of geotechnical structures and has to be reproduced by constitutive models. Many researchers have investigated the influence of stress history and sample preparation on the mechanical behaviour of saturated fine-grained soils covering mainly K_0 or $p' = \text{const.}$ preloading paths [30, 39, 59, 69–71]. The influence of an undrained shearing path either in compression or in extension up to different shear stresses on the mechanical response was investigated for sand in, e.g. [25, 31]. Nevertheless, such studies for fine-grained soils are rare to find in literature. Therefore, the purpose of this study is to bridge this gap and provide valuable insights in this area.

In [74] a comprehensive database with results from undrained cyclic laboratory tests with varying boundary conditions and load characteristics performed on a kaolin is available. These experimental results reveal different inclinations of effective stress paths for specimens cut out in different directions with respect to the sedimentation axis. Wichtmann et al. [74] included also experiments with monotonic loading, but these were restricted to triaxial compression. In order to evaluate the influence of the inherent anisotropy i.e. initial secant stiffness anisotropy (which means anisotropic stiffness tensor) also in triaxial extension, the experiments from [74] are supplemented here. In this study, the term initial secant stiffness refers to the stiffness evaluated at small strain levels within the linear portion of the stress–strain response obtained from the triaxial tests, and should not be confused with small-strain stiffness derived from seismic or bender element methods. Furthermore, additional tests with different preloading histories in both triaxial extension and triaxial compression under undrained conditions are presented, allowing the stress ratio to develop freely. With these experiments, the transformation of the inherent anisotropy with preshearing is inspected and some novel findings depending on the cutting direction of the samples as well as preloading deviator stress level are reported. Furthermore, these experiments can be used for the validation and development of constitutive models, particularly with respect to preloading effects on the shear strength, and the dependence of yield surface and internal variables on the cutting direction of the samples, overconsolidation ratio and preloading direction (isotropic compression or undrained preshearing) and magnitude. In this work, the term *yield surface* denotes the current stress boundary associated with the onset of irreversible deformation, as commonly defined in elastoplasticity. In contrast, the *preconsolidation surface* refers to the historical stress limit resulting from previous loading, as used in hypoplasticity and bounding surface plasticity. These two surfaces fulfil different conceptual roles and therefore do not necessarily coincide.

Additionally, this study incorporates a numerical component based on the anisotropic visco-hypoplastic (AVHP) model by [41], extended to account for strength anisotropy, allowing for a detailed comparison between numerical simulations and the experimental results. To better capture the influence of inherent anisotropy on stiffness, the AVHP model has been further enhanced by incorporating a cross-isotropic elastic stiffness formulation. By increasing the number of parameters and model complexity, this approach enables a systematic evaluation of the key parameters and mathematical formulations essential for describing the anisotropic behaviour of fine-grained soils. Furthermore, numerical simulations were also conducted using the widely used modified Cam Clay (MCC) model [50] and the original AVHP model by [41] to provide a comparative framework.

The MCC model was deliberately chosen despite its well-documented limitations in capturing inherent anisotropy, as it serves as a valuable baseline for comparison. As a widely used elastoplastic model in geotechnical engineering, particularly for describing clay behaviour, MCC provides an effective reference point for identifying the shortcomings of traditional models.

The AVHP model was selected due to its proven ability to account for both viscous and anisotropic behaviour, aligning closely with the experimental conditions of this study. This combination of models facilitates a balanced evaluation, comparing a conventional elastoplastic approach with a specialised anisotropic-viscous framework, ultimately demonstrating the added predictive power of incorporating anisotropy in advanced constitutive models.

2 Symbols and Notation

In this article, vectors and second-order tensors are represented with bold symbols, for example the effective Cauchy stress $\boldsymbol{\sigma}$ and strain $\boldsymbol{\varepsilon}$. $||\boldsymbol{X}|| = \sqrt{\operatorname{tr}\ \boldsymbol{X}^2}$ is the Frobenius norm of $\boldsymbol{X}$, $\operatorname{tr}\ \boldsymbol{X}$ is the sum of the diagonal components of

$\boldsymbol{X}$. Cauchy stresses are considered as effective ones. $\mathring{\boldsymbol{\sigma}}$ is the co-rotational, objective stress rate. The strain tensor $\boldsymbol{\varepsilon}$ is the symmetric part of the velocity gradient.

In a conventional triaxial test the axial stress is denoted with σ'_1 (assuming compression as positive, and extension as negative) and the radial stress is denoted with $\sigma'_2(=\sigma'_3)$. The associated strains are ε_1 and $\varepsilon_2 = \varepsilon_3$. The Roscoe invariants for triaxial conditions are defined as $p' = (\sigma_1 + \sigma_2 + \sigma_3)/3$, $q = (\sigma_1 - \sigma_2)$ and $\varepsilon_p = (\varepsilon_1 + \varepsilon_2 + \varepsilon_3)/3$, $\varepsilon_q = -2/3 \cdot (\varepsilon_1 - \varepsilon_2)$. Initial values are labelled with the subscript $\sqcup'_0$. The deviatoric part of a tensor is denoted by a superscript asterisk. For instance, the deviatoric effective stress is expressed as $\boldsymbol{\sigma}'^{*} = \boldsymbol{\sigma}' - p'\mathbf{1}$.

Any symmetric second-order tensor can be written as vector with the principal values $\boldsymbol{X}_{\mathrm{v}} = [X_1, X_2, X_3]$. Bold calligraphic letters denote fourth-order tensors (e.g. $\mathcal{M}$). Tensor operations are written following the Einstein summation convention. In particular, the indices follow the lexicographic order: $\boldsymbol{X} \otimes \boldsymbol{Y} = X_{ij}Y_{kl}$, $\boldsymbol{X} : \boldsymbol{Y} = X_{ij}Y_{ij}$ and $\mathcal{L} : \boldsymbol{\varepsilon} = \mathcal{L}_{ijkl}D_{kl}$. Second-order unit tensor $\mathbf{I}$ is defined as $I_{ij} = \delta_{ij}$ and the fourth-order tensor $\mathcal{I}$ as $\mathcal{I}_{ijkl} = \delta_{ik}\delta_{jl}$, using the Kronecker delta symbol δ_{ij}.

3 Laboratory tests

The present section presents the new laboratory tests conducted on kaolin along with the previous results shown in [74] and a respective discussion. The kaolin used in the new tests is identical to the one tested by [74]. Thus, the additional experiments presented herein are directly comparable to the ones included in the database on the website of the fourth author (torsten-wichtmann.de) and serve constitutive modellers to validate and develop further their equations especially with respect to stiffness anisotropy (e.g. different Young's modulus in vertical and horizontal direction), and the influence of drained and undrained preloading on the mechanical behaviour of fine-grained soils.

3.1 Material and sample preparation

Table 1 Index properties of kaolin

Grain density ρ_s	Liquid limit w_L	Plastic limit w_P	Plasticity index I_p	Clay fraction ($d < 2$ µm)
2.675 gcm^{-}3	47.2%	35.0%	12.2%	35.0%

All presented element tests were conducted on kaolin powder (Kaolin K1 of the company Gebrüder Dorfner GmbH & Co. KG) which can be classified as medium-plastic silt according to Casagrande's I_p-w_L-Diagramm. Table 1 summarises the results of index tests on the material also referred to as Karlsruhe kaolin in literature [13]. The grain size distribution can be found in Fig. 1. For sample preparation, the kaolin powder is mixed with water to obtain a slurry with a water content w being 2.5 times the liquid limit w_L ($w = 2.5 \cdot w_L$). After mixing the slurry, it is pre-consolidated in a plexiglas cylinder with an inner diameter of $d = 130$ mm applying a maximum vertical stress $\sigma_{\mathrm{v,max}} = 100$ kPa, leading to a sample height of $h \approx 130$ mm. Afterwards, triaxial samples with dimensions $d = h = 50$ mm are cut out of the centre of the pre-consolidated kaolin sample (see Fig. 2a, b), following the same procedure as in [74]. Samples, prepared with this procedure and material, was shown to be homogenous by comparing the water content of different cubes cut from the preconsolidation cylinder [74]. After K_0-consolidation in the pre-consolidation cylinders, the samples are unloaded during cutting and trimming and afterwards isotropically reconsolidated. The recommended height of two times the diameter (ensuring neglectable influence of the endplates) could be reduced using smeared endplates with a filter stone in the middle. The reduced height of the sample leads to shorter consolidation time. The method was applied on former experimental studies as well, e.g. [74] and a comparison with higher samples was carried out on a Norwegian clay in [73].

The material exhibited inherent anisotropy in the experimental study of [74], which involved undrained triaxial loading at different initial mean effective pressures on samples that were initially isotropically and normally consolidated. A higher stiffness was observed in the horizontal direction than in the vertical one, attributed to the preferred particle orientation (Fig. 2d). To analyze this behaviour also in the current study, samples cut out in horizontal direction from the pre-consolidated cylinders are examined as well. For these samples in a first step a cube is cut out vertically from the pre-consolidated sample as presented in Fig. 2c. Afterwards the cube is rotated by 90° before cutting the final triaxial sample out of the cube. Additionally, a sample cut out in diagonal direction, i.e. 45°, is considered.

Finally, the sample was mounted into the triaxial device. A backpressure in the pore water of 500kPa was used. The saturation of the specimens was verified using the Skempton parameter B. In all tests, the criterion $B > 0.95$ was satisfied, in accordance with DIN EN ISO 17892-9 [8]. The performed monotonic triaxial compression and extension tests as well as experiments with different preloading steps are discussed in Sects. 3.2 and 3.3,

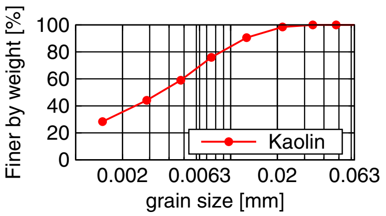

Fig. 1 Grain size distribution of the ground kaolin powder

respectively. The final undrained shearing stage was conducted up to 20–25% axial strain, with all tests exhibiting strain localization as the dominant large-deformation mechanism. Approximately 30% of the tests were repeated, demonstrating satisfactory reproducibility.

3.2 Monotonic triaxial tests

[74] discovered that the tested material presents an inherent anisotropy arising from the deposition mode and shape of the particles. This was shown by employing different cutting directions of the tested specimen under undrained triaxial compression. In this work, those experiments, along with new ones under different loading conditions including triaxial extension, are presented. To investigate the influence of the sample's cutting direction on its mechanical behaviour, Fig. 3 shows triaxial compression tests on samples cut out vertically, horizontally (for reproduction purposes), and at a 45° angle (from [72]). Both, the sample with a horizontal and 45° cutting direction show a less contractant behaviour than the vertically cut out sample and therefore reach a higher shear strength. The stress path of the sample with a cutting direction of 45° lies between the one of the horizontally and the vertically cut out sample. Therefore, the vertical and horizontal cutting direction are presumed to be the two limit cases, between which the other cutting directions may lie. For the further test series only samples with horizontal and vertical cutting directions will be used.

An overview of the monotonic test series is given in Table 2. Hereby, the database of [74] (M02–M05 in Table 2) is extended by respective experiments in both triaxial extension and compression with samples cut out either in horizontal or vertical direction as listed in Table 2. In this series of tests the samples were isotropically consolidated to different effective mean pressures $p'_0 = \{100, 200, 300, 400\}$ kPa. After the completion of consolidation under the desired mean pressure, the drainage was closed and the vertical displacement was increased or decreased to match triaxial compression or extension conditions, respectively. The displacement was controlled

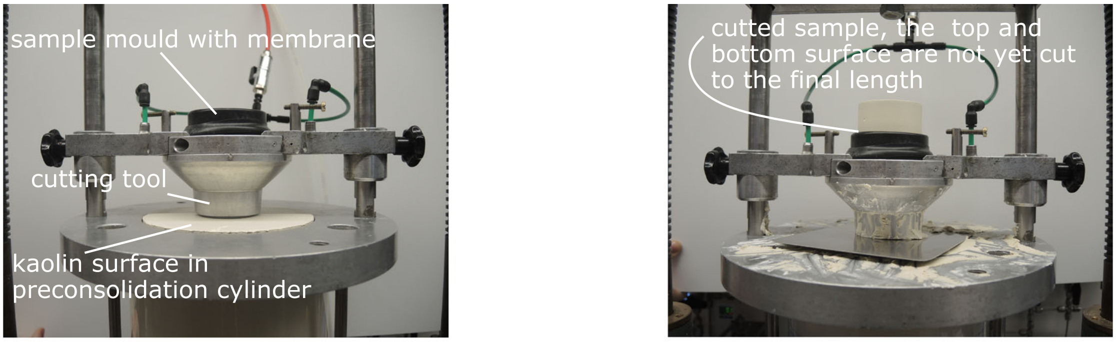

(a) Kaolin in preconsolidation cylinder prepared for cutting the sample

(b) Cutted sample from preconsolidation cylinder, end surfaces are not yet prepared

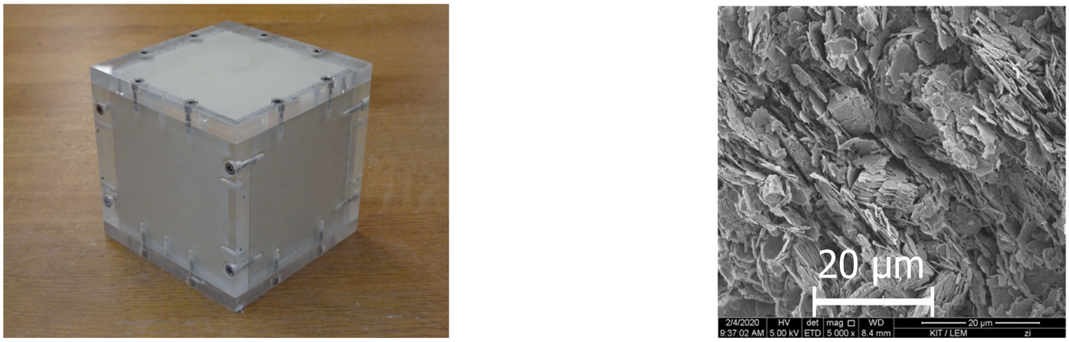

(c) Cutted cube to produce samples with horizontal cutting direction

(d) SEM microscopy of a dried kaolin sample

Fig. 2 Sample preparation

with a constant rate of $\dot{s} = 0.025\,\mathrm{mm/min}$ ($\dot{\varepsilon} \approx 0.05\%/\mathrm{min}$) in all tests. Note that all loading paths with a change in deviator stress have been performed under isochoric (undrained) conditions, whereas the paths along the isotropic axis (in Sect. 2.3) have been performed by open drainage (hence under drained conditions).

Fig. 4a shows the effective stress paths of all monotonic tests in the $p' - q$ plane. The corresponding $q - \varepsilon_1$ diagram is given in Fig. 4b. The tests on samples cut out in vertical direction (red) are compared to tests on samples cut out in horizontal direction (orange). The stress paths of the compression tests on vertically cut out samples are inclined to the upper left of the $p' - q$ diagram and show contractive behaviour, i.e. a reduction of the effective mean pressure p' because of increasing pore water pressure Δu except the final stage. When approaching the maximum deviator stress a drop of the shear strength of approx. 5–20 kPa (increasing with the initial mean effective stress) is experienced. At this stage the axial strain has already reached large values $\varepsilon_1 > 15\%$, hence a homogeneous strain distribution within the sample cannot be guaranteed anymore. The samples with a horizontal cutting direction respond less contractive, show a steeper effective stress path and therefore reach a slightly higher deviator stress when sheared under triaxial compression.

In triaxial extension the behaviour is opposite to the one of the compression tests. All samples sheared under triaxial extension show a prevented contractancy after an initial prevented dilatancy, which contrasts the purely contractive tendencies in the triaxial compression tests. Furthermore, the samples cut out in vertical direction show steeper effective stress paths resulting in an increased shear strength compared to horizontally cut out samples. The instant drop of the deviator stress indicating localisation of shear strains starts already at an axial strain of $\varepsilon_1 > 7\%$ in triaxial extension, especially for vertically cut out specimens.

Table 2 Test program on normally consolidated samples with a displacement rate of $\dot{s} = 0.025\mathrm{mm/min}$ (strain rate $\dot{\varepsilon} \approx 0.05\%/\mathrm{mm}$), tests M02–M05 from [74]

Test	Cutting direction	p'_0 kPa	Triaxial	e_0
M02	Vertical	100	Compression	1.332
H100K	Horizontal	100	Compression	1.248
V100E	Vertical	100	Extension	1.281
H100E	Horizontal	100	Extension	1.248
M03	Vertical	200	Compression	1.332
V200E	Vertical	200	Extension	1.247
M04	Vertical	300	Compression	1.244
H300K	Horizontal	300	Compression	1.087
M05	Vertical	400	Compression	1.214
V400E	Vertical	400	Extension	1.061
H400E	Horizontal	400	Extension	1.004

The increase of undrained shear strength in triaxial compression for horizontally cut out samples compared to samples cut out in vertical direction is in good agreement with the triaxial compression tests presented in [4, 33]. [4] further reports a strong influence of particle-size gradation, which means the silt content, the clay content, and the plasticity index on the anisotropic stress–strain and strength characteristics of vertical and horizontal triaxial specimens of cohesive, fine-grained soils, including the comparable kaolin clay from Connecticut, New Canaan. On the other hand, [33] observed the lowest strength for an inclination angle of 60° between the consolidation axis and

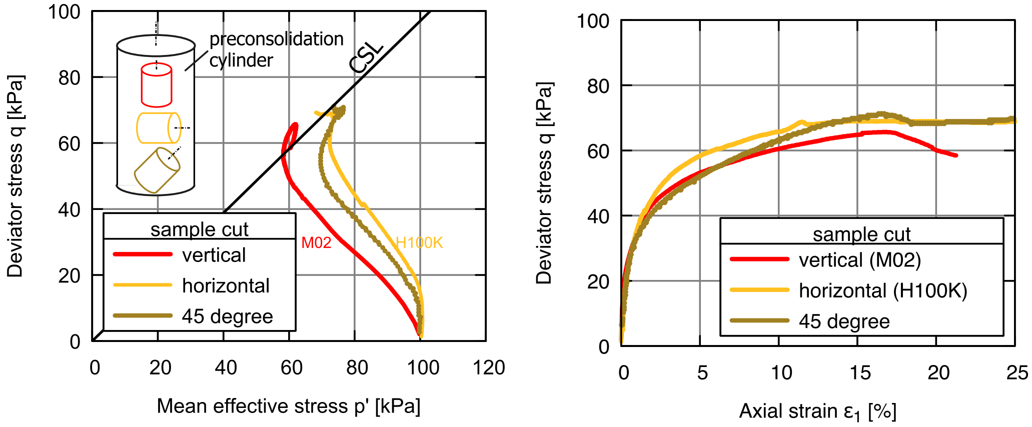

(a) Effective stress paths in the p'-q plane

(b) Deviator stress q vs. axial strain ε_1
Corrected strain for the sample under 45° due to issues with the interconnection of the loading piston

Fig. 3 Monotonic triaxial tests on kaolin with vertically and horizontally cut out samples. CSL denotes the critical state line the vertical axis of the triaxial device. In contrast, the results presented in Fig. 3 reveal that for the considered kaolin samples, the highest undrained shear strength is observed in specimens extracted with a horizontal cutting direction (0°). The undrained shear strength of specimens prepared with a 45° cutting direction appears to fall between the values obtained for horizontally (0°) and vertically (90°) oriented samples. While this suggests a potential correlation between the cutting direction and the shear strength, additional experimental data are required to substantiate and further elucidate the observed trends. In this regard, Toyota et al. [70] describe a dependency of the undrained shear strength from the angle $\Delta\alpha$ between the major principal stress during preconsolidation and during shearing based on hollow cylinder experiments. Thereby, the undrained shear strength increased with decreasing $\Delta\alpha$. A representation of $\Delta\alpha$ for the loading and boundary conditions considered in this work is given in Fig. 5. In the case of a vertically cut out sample, the major principal stress directions during preconsolidation and shearing in triaxial compression are aligned ($\Delta\alpha = 0°$), whereas for shearing in triaxial extension, they are perpendicular ($\Delta\alpha = 90°$). Conversely, for horizontally cut out samples, the opposite holds: in triaxial compression, $\Delta\alpha = 90°$, while in triaxial extension, $\Delta\alpha = 0°$ (see Figs. 5 and 4). The experiments in this study indicate an increase in shear strength with increasing $\Delta\alpha$, i.e., higher shear strength for $\Delta\alpha = 90°$ (see Fig. 4), which contradicts the results presented by [70]. This may be due to the different materials or the differences in the preconsolidation. The samples in [70] where pre-consolidated under K_0 conditions and prior to undrained shearing were subjected to an undrained reduction of deviator stress until the p-axis was reached (i.e. $q = 0$ kPa). Hence, even though both experiments start from an isotropic stress state, the preconsolidation history

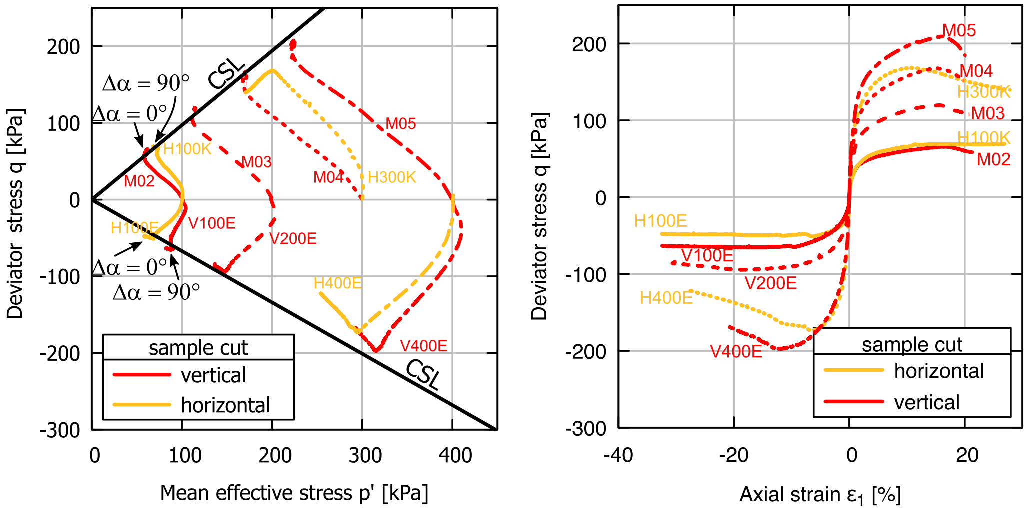

(a) Effective stress paths in the p'-q plane

(b) Deviator stress q vs. axial strain ε_1

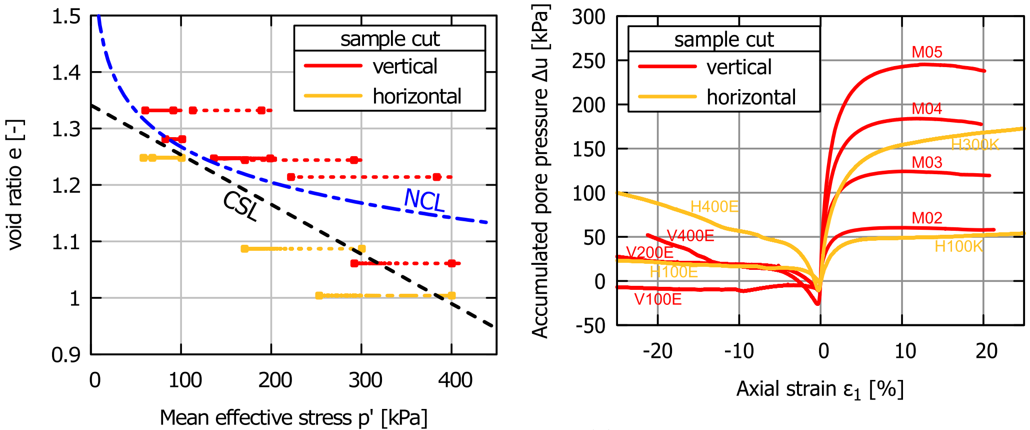

(c) Void ratio vs. mean effective stress p'

(d) Excess pore pressure Δu vs. axial strain ε_1

Fig. 4 Monotonic triaxial tests on kaolin with vertically and horizontally cut out samples

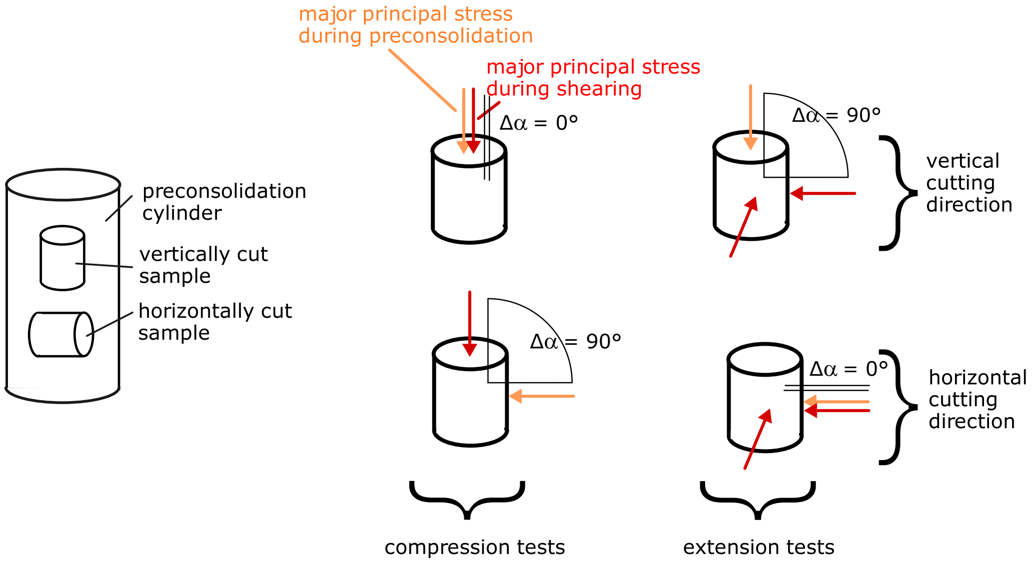

Fig. 5 Overview of presented combinations of cutting direction of the sample, major principal stress direction during preconsolidation and during final shearing

Table 3 Presented triaxial tests with different preshearing histories. All tests were conducted on vertically cut out samples with a displacement rate of $\dot{s}$ =0.025 mm/min (strain rate $\dot{\varepsilon} \approx 0.05\%$/min)

Test	Triaxial	$p'_{0,0}$ kPa	$p'_{0,1}$ kPa	$p'_{0,2}$	$e_{0,1}$	$e_{0,2}$	OCR_1	OCR_2
Comp2	Compression	500	500	400	1.069	1.065	1.00	1.25
Comp3	Compression	300	300	150	1.167	1.165	1.00	2.00
Comp4	Compression	500	200	500	1.049	0.991	2.50	1.00
Ext 2	Extension	500	200	500	1.052	0.972	2.50	1.00
Ext 4	Extension	500	500	400	1.037	1.041	1.0	1.25

is different and may lead to a distinct behaviour in the shear strength as will be observed in Sect. 3.3.

3.3 Triaxial tests with preshearing history

The mechanical behaviour of soils depends on many factors. One of them is the stress and strain history. In the following, triaxial tests with different prealoading histories are presented to examine the stress induced change of inherent anisotropy of this kaolin. Each test contains two undrained triaxial compression or triaxial extension loading phases. Thereby, in the same test two undrained shear paths with the same direction of axial deformation take place on various effective mean pressures $p'_{0,1}$ and $p'_{0,2}$ corresponding to overconsolidation ratios $\mathrm{OCR}_1 = p'_{0,0}/p'_{0,1}$ and $\mathrm{OCR}_2 = p'_{0,1}/p'_{0,2}$, respectively. For each sample, the values of the mean stresses $p'_{0,1}$ and $p'_{0,2}$ prior to the shearing phases are listed in Table 3 together with the initial confining pressure $p'_{0,0}$. The void ratios reached after consolidating the sample under $p'_{0,1}$ and $p'_{0,2}$ are referred to as $e_{0,1}$ and $e_{0,2}$, respectively. On the first starting pressure $p'_{0,1}$ the axial displacement is increased (or decreased) under undrained conditions. At the end of this shearing phase, the direction of displacement is reversed until the isotropic line is reached, hence the deviator stress takes the value $q_{0,2} = 0$ kPa. Now, during control of the deviator stress $q_{0,2} = 0$ kPa the drainage is opened and the sample is isotropically loaded or unloaded under drained conditions until $p'_{0,2}$. After consolidation at the second confining pressure $p'_{0,2}$ the axial displacement is increased (or decreased) under undrained conditions until failure. In some of the tests the effective mean pressure p' is increased and decreased before the first or between the two axial displacement steps to manipulate the over consolidation ratio OCR as specified in Table 3. All other conditions as, e.g. back pressure, displacement rate and sample dimension coincide with those presented in Sect. 3.3.

The test Comp2 presented in Fig. 6 starts with a consolidation phase reaching the pressure $p'_{0,1} = 500$ kPa. The following shearing applied under undrained conditions, which compresses the sample, is stopped at $q = 200\,\mathrm{kPa}$. Then the deviator stress is reversed until an isotropic state is reached. The second triaxial compression step starts from the confining pressure $p' = 400\,\mathrm{kPa}$ and $q = 0$ corresponding to an overconsolidation ratio of $\mathrm{OCR}_2 = p'_{0,1}/p'_{0,2} = 1.25$. The second effective stress path shows a steeper slope than the path without preloading steps (grey line). However, the soil response is still contractive, i.e. effective stress continuously decreases during undrained shearing. When the deviator stress reaches the value $q = 200\,\mathrm{kPa}$, hence the maximum deviator stress the sample has experienced in the past, the stress path shows a kink and approaches the gradient of the path without preloading. Hence, at this stage the specimen exceeds the highest preloading stress and thus reaches the normally consolidated envelope ($\mathrm{OCR} = 1$) and behaves like a virgin specimen in further loading path (compare with the slope of the path without preloading). At the end of the test with preshearing, the same critical state line (CSL) as for the monotonic tests without preloading is reached. Even though, the overall shear strength is approx. 30% higher than the one without preloading. These relationships may serve as a valuable indicator for the estimation of a fast preshearing magnitude of a fine-grained soil in order to obtain a required stiffness (and reduce the settlements) as well as a case study for sophisticated constitutive models.

The test Ext4 illustrated in Fig. 7 includes the same confining pressures as Comp2, while the undrained shearing is applied in triaxial extension. The first loading step starting from the consolidation pressure $p'_{0,1} = 500\,\mathrm{kPa}$ is

Table 4 Parameters of MCC for Karlsruhe kaolin

ν	κ	λ	M
0.33	0.05	0.13	0.942

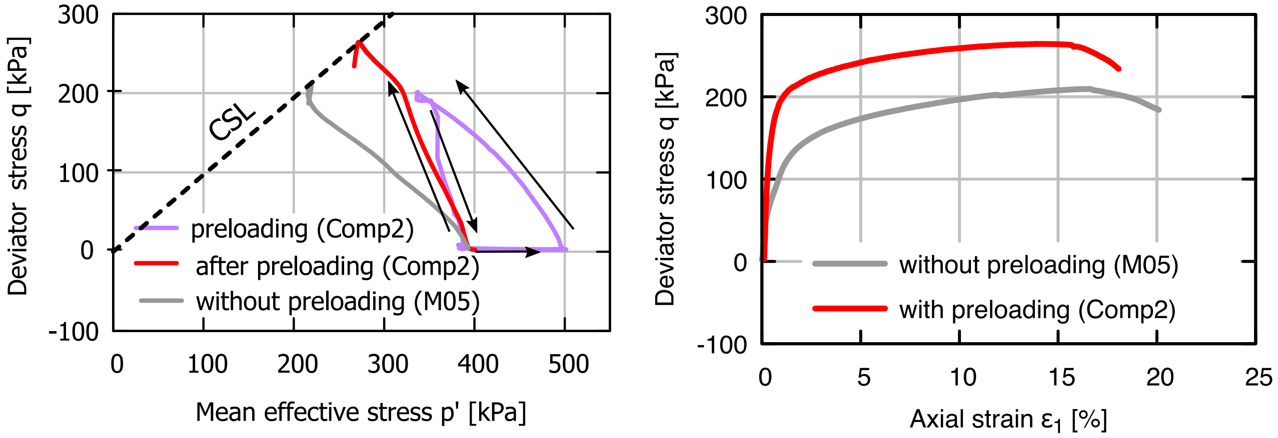

(a) Effective stress paths in the p'-q plane (b) Deviator stress q vs. axial strain ε_1

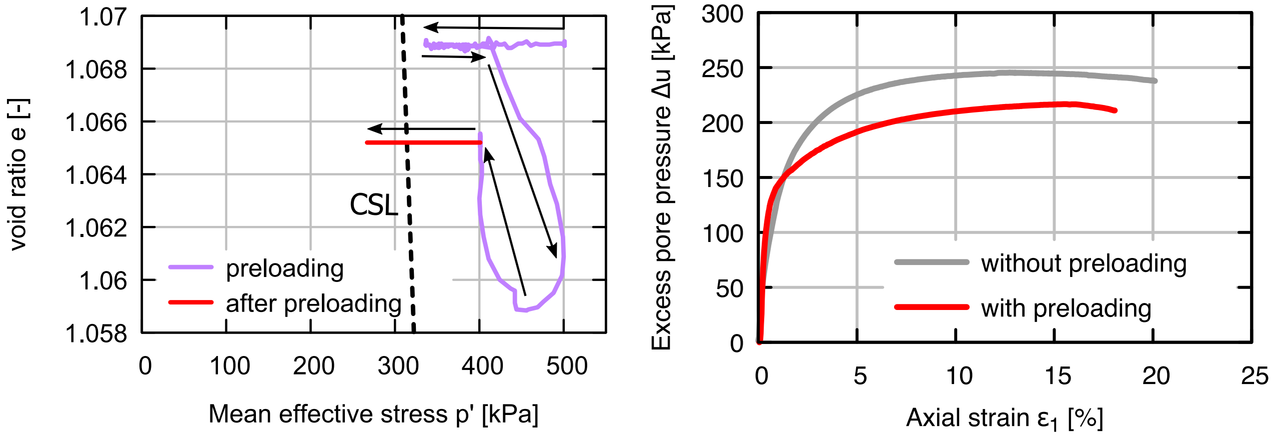

(c) Void ratio vs. mean effective stress p' (d) Excess pore pressure Δu vs. axial strain ε_1

Fig. 6 Comparison between the triaxial test Comp2 with a preshearing path and the monotonic triaxial test M05 without preloading. All tests are conducted on samples cut out in vertical direction

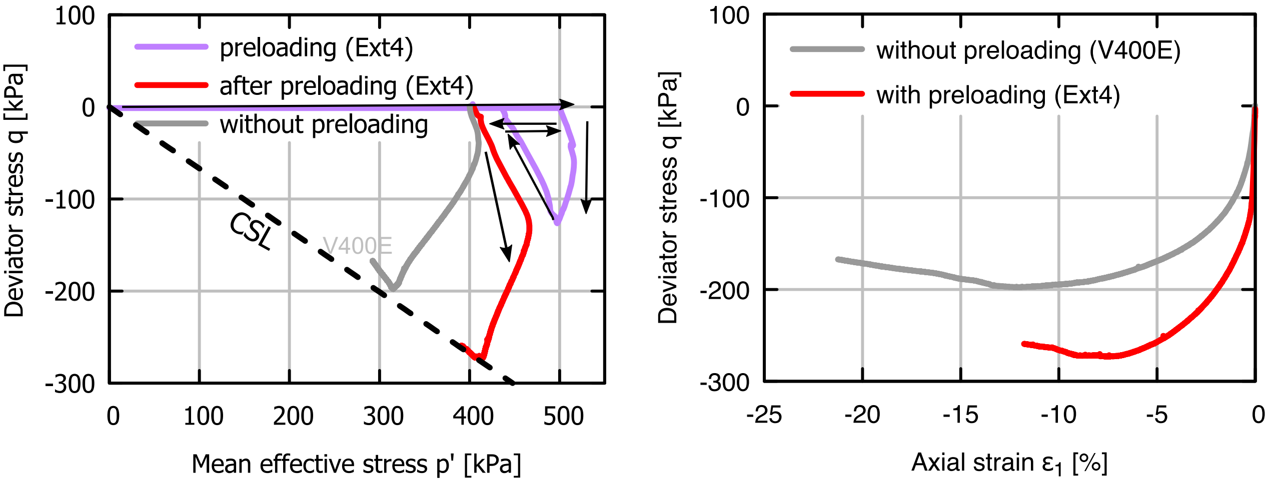

(a) Effective stress paths in the p'-q plane

(b) Deviator stress q vs. axial strain ε_1

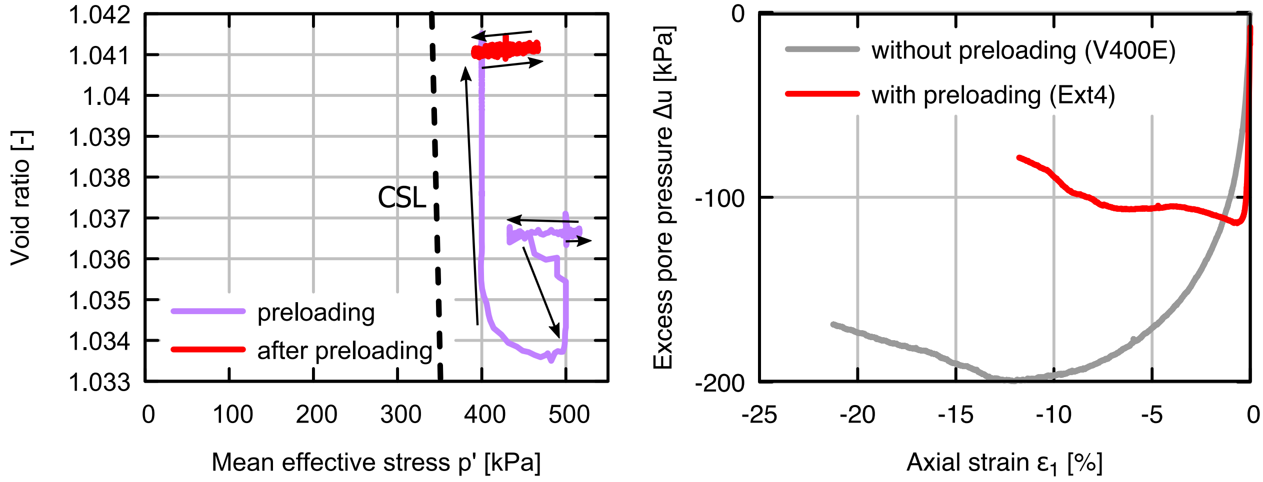

(c) Void ratio vs. mean effective stress p'

(d) Excess pore pressure Δu vs. axial strain ε_1

Fig. 7 Comparison between the triaxial test Ext4 with a preshearing path and the monotonic triaxial test V400E without preloading. All tests are conducted on samples cut out in vertical direction

Table 5 Parameters of the reference and extended (additional α, β) AVHP model for Karlsruhe kaolin

e_{100}	λ^*	κ^*	I_v	D_r (s^{-1})	φ_c (°)	C_1	C_2	C_3	α	β
1.2	0.08	0.07	0.015	10^{-6}	24	0.0015	600	0.618	1.8	1.2

reversed when the deviatoric strain q takes the value $-126\,\mathrm{kPa}$. The stress path of the second loading starting from $p'_{0,2} = 400\,\mathrm{kPa}$ resembles the observations of the corresponding path of Comp2: after reaching the maximum deviator stress of the first loading step a bend is evident and the gradient of the effective stress path now approaches the slope of the corresponding path without preloading. Until reaching the maximum deviator stress of the first loading step the stress path shows a dilative tendency accompanied by an increase of mean effective stress, leading to a higher shear strength at the end of the test compared to the test without preloading. The increase in shear strength in triaxial extension amounts approx. 40% compared to the path without preloading. The axial strain at which the peak is reached is rendered lower for the test with preloading, see

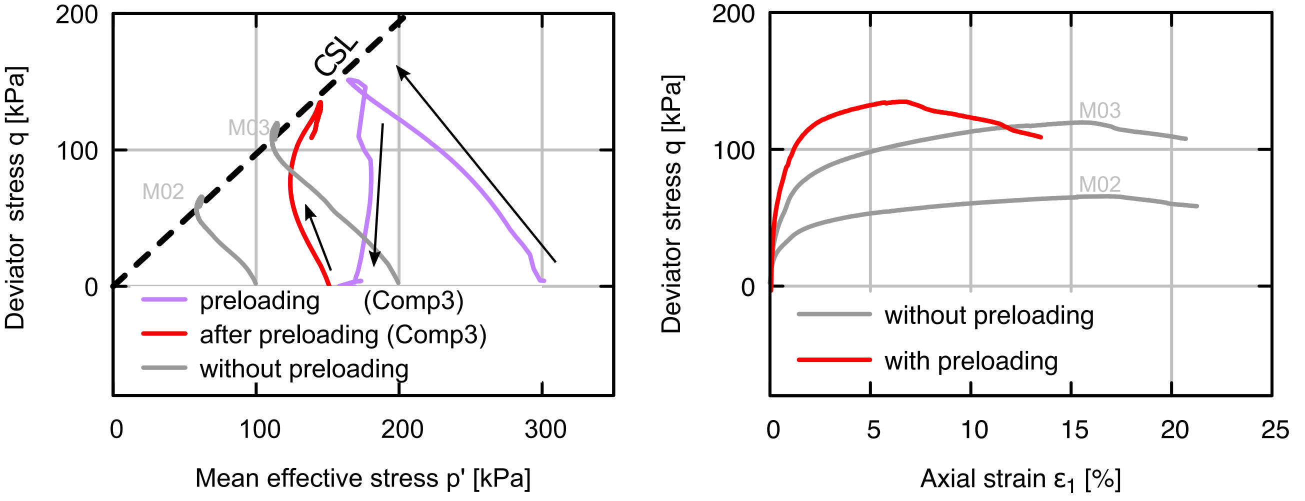

(a) Effective stress paths in the p'-q plane (b) Deviator stress q vs. axial strain ε_1

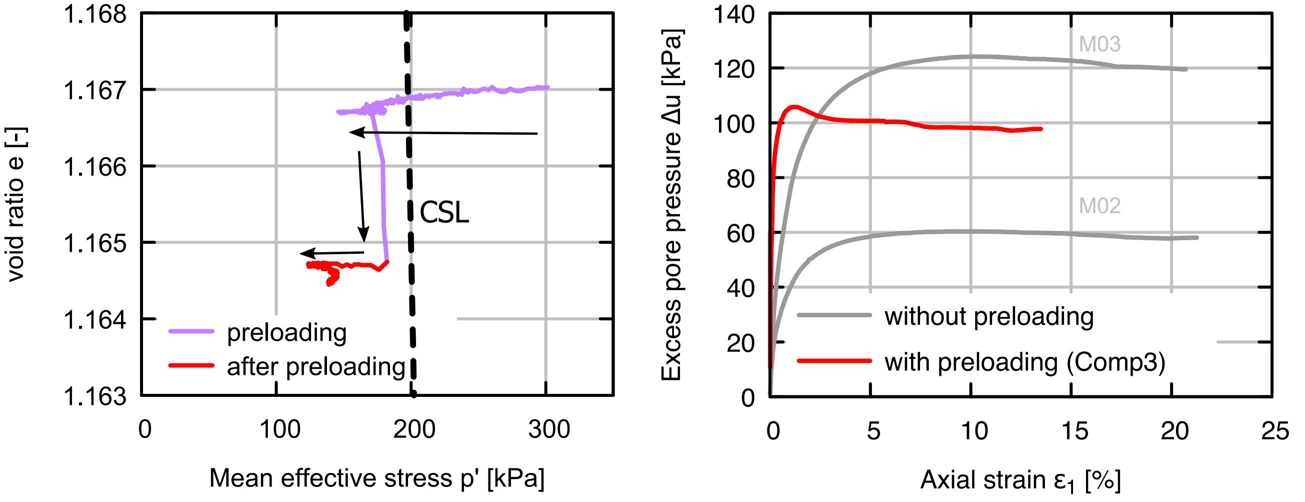

(c) Void ratio vs. mean effective stress p' (d) Excess pore pressure Δu vs. axial strain ε_1

Fig. 8 Comparison between the triaxial test Comp3 with a preshearing path and the monotonic triaxial tests M02 and M03 without preloading. All tests are conducted on samples cut out in vertical direction

Fig. 7b Hence, a preloading increases the stiffness of the specimen in the respective direction.

The consolidation pressures $p'_{0,1} = 300$ kPa and $p'_{0,2} \approx 150$ kPa of the test Comp3 in Fig. 8 with two triaxial compression steps are lower than those of Comp2 and Ext4. The first shearing in triaxial compression is reversed at $q = 151$kPa slightly before the CSL is reached. After reconsolidation to $p' = 150$ kPa and $q = 0$ (resulting in an isotropic overconsolidation ratio of $\mathrm{OCR}_2 = 2.00$) the second shearing step takes place. Again, the second stress path shows a steeper slope than the paths without preloading and the behaviour changes from contractant to dilatant during undrained shearing, which is expected for overconsolidated fine-grained soils [74]. There is no kink of the stress path followed by a more contractive behaviour similar to the test Comp2 because the foregoing shearing almost reached the CSL. The initial stiffness is increased by preloading (see Fig. 8b), while a sudden softening behaviour of the deviator stress is observed already at $\varepsilon_1 > 7.5\%$ probably due to shear band formation.

In both tests Comp4 (Fig. 9) and Ext2 (Fig. 10) the first loading step commenced at a lower confining pressure ($200\,\mathrm{kPa} = p'_{0,1} < p'_{0,2}$) than the second one. The axial loading steps of Comp4 are compression paths. The test starts with an isotropic consolidation to $p' = 500$ kPa, followed by an isotropic unloading to the first confining pressure $p'_{0,1} = 200$ kPa. Therefore the specimen has an overconsolidation ratio of $\mathrm{OCR} = 2.5$. The resultant effective stress path in Fig. 9 is less contractive than the one without isotropic preloading. Subsequently, the axial

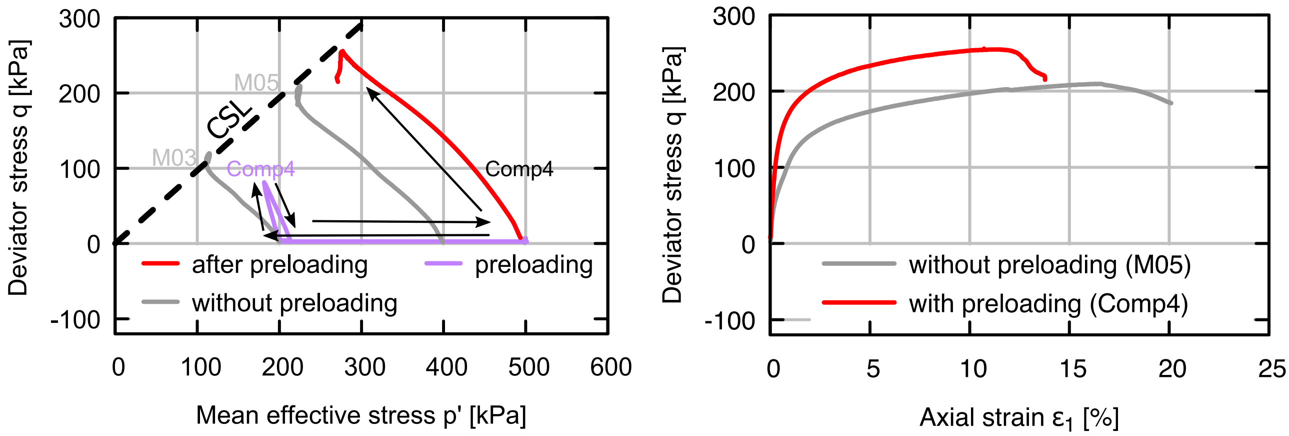

(a) Effective stress paths in the p'-q plane (b) Deviator stress q vs. axial strain ε_1

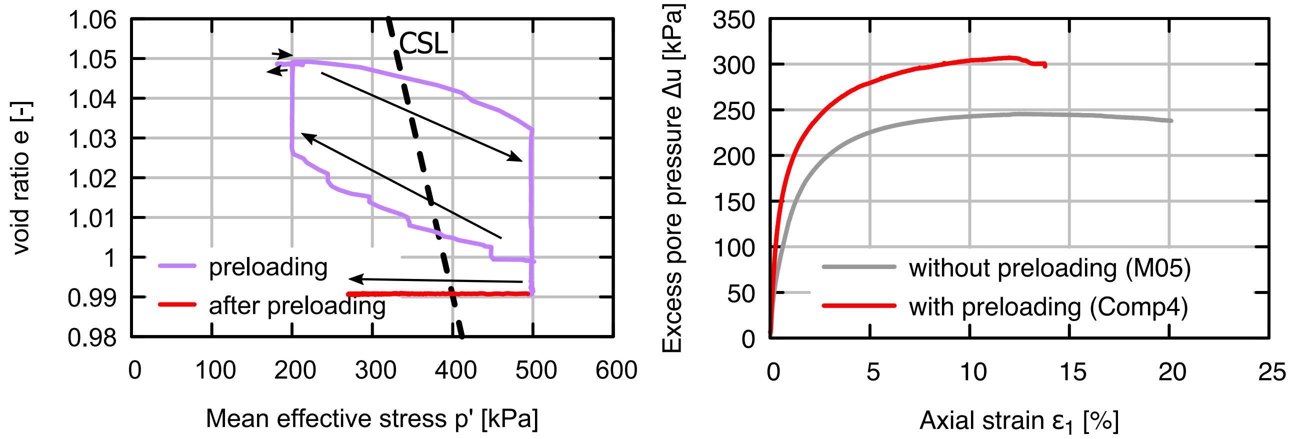

(c) Void ratio vs. mean effective stress p' (d) Excess pore pressure Δu vs. axial strain ε_1

Fig. 9 Comparison between the triaxial test Comp4 with a preshearing path and the monotonic triaxial tests M03 and M05 without preloading. All tests are conducted on samples cut out in vertical direction

deformation is reversed at $q = 82\,\text{kPa}$ before reaching the phase transformation line (the lines at which the soil behaviour changes from contract to dilatant). After reconsolidation to the second consolidation pressure $p'_{0,2} = 500\,\text{kPa}$ corresponding to $\text{OCR}_2 = 1.0$, the sample is sheared in triaxial compression until failure. As expected for $\text{OCR} = 1.0$, the gradient of the corresponding stress path is similar to the one of a compression test without preloading. Hence, the induced anisotropy of this specimen is rendered rather low due to the low magnitude of preshearing.

The test Ext2 also starts with $\text{OCR}_1 = 2.5$ and $p'_{0,1} = 200\,\text{kPa}$. Here the sample is first subjected to a triaxial extension path until the deviator stress is reversed almost at the CSL with $q = -162\,\text{kPa}$. The first undrained shearing results in a dilatant effective stress path due to the overconsolidation of the specimen. The second shearing commenced at an isotropic state with $p'_{0,2} = 500\,\text{kPa}$ corresponding to $\text{OCR}_2 = 1.0$. The final stress path was still found influenced by the former preshearing until approaching the CSL, with the sample showing almost completely dilatant behaviour. Note that in the case without preshearing (grey line in Fig. 10a) the change between the dilative phase at the beginning and the contractive phase afterwards is rendered abruptly.

The overconsolidation ratio as well as the previous preshearing plays an important role on the overall behaviour of the material as well as on its shear strength. While the increase of the shear strength with OCR as well as the arising dilatancy are commonly expected, the influence of preshearing on the inherent anisotropy and thus on the stiffness is dependent on the magnitude of preshearing. Figure 11 presents a summary of all effective stress paths of samples cut out in vertical direction, whereby different conclusions can be made. First the distinct slopes of the paths at $p'_0 = p'_{0,1} = 200$ kPa in triaxial extension can be

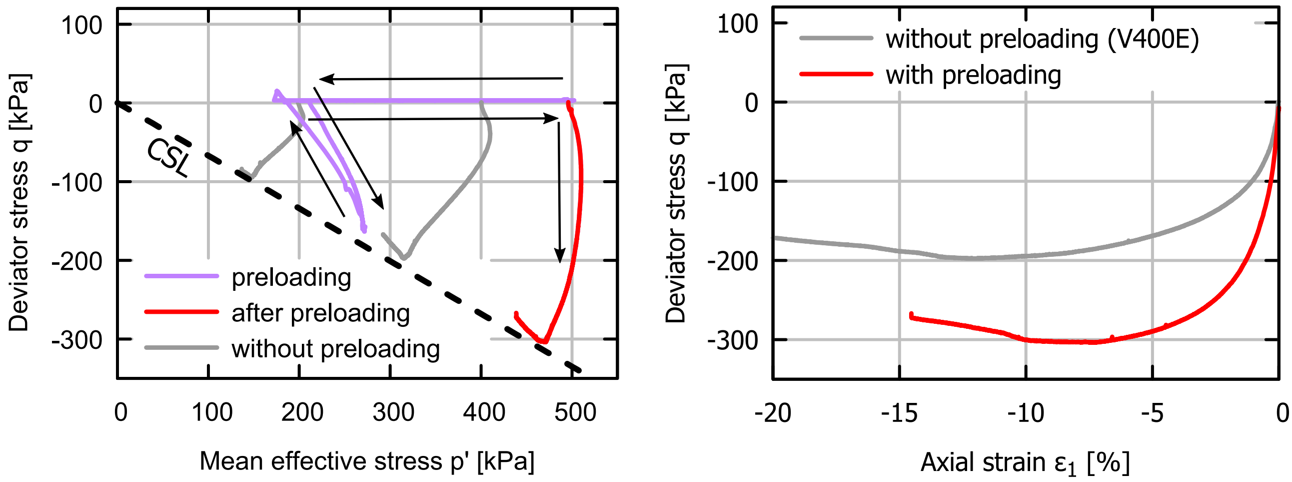

(a) Effective stress paths in the p'-q plane

(b) Deviator stress q vs. axial strain ε_1

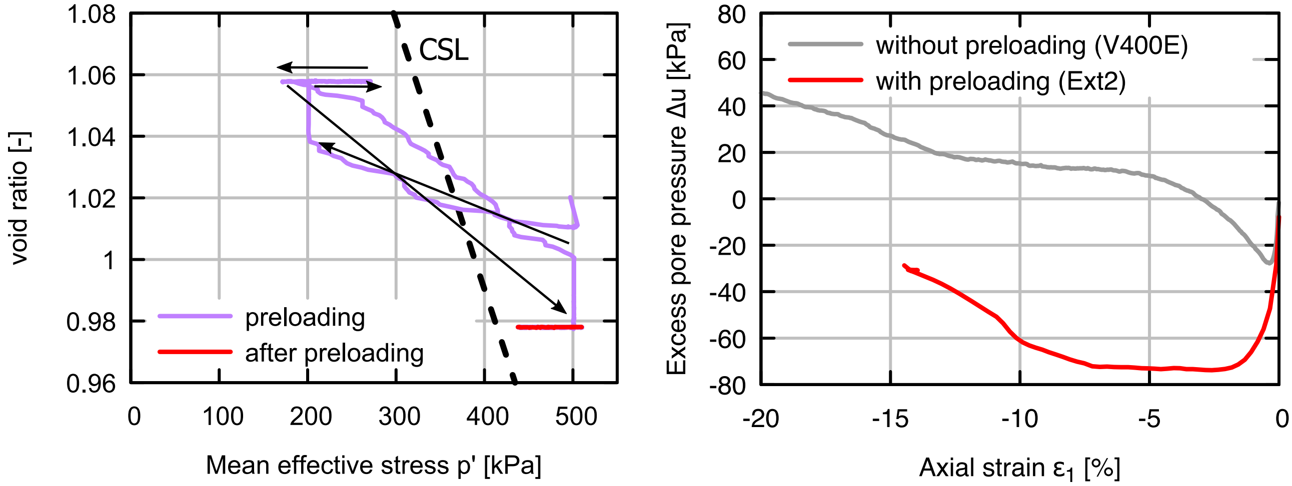

(c) Void ratio vs. mean effective stress p'

(d) Excess pore pressure Δu vs. axial strain ε_1

Fig. 10 Comparison between the triaxial test Ext2 with a preshearing path and the monotonic triaxial tests V200E and V400E without preloading. All tests are conducted on samples cut out in vertical direction

attributed to the influence of initial precompression of the sample in Ext2 to $p' = 500$ kPa rendering $\mathrm{OCR}_1 = 2,5$ kPa. Secondly, the stress paths at $p'_0 = p'_{0,2} = 400$ kPa either in triaxial extension or in triaxial compression show clearly that the slope of the effective stress path, thus the initial secant stiffness as well, is influenced by the previous preshearing. Until reaching the maximum deviator stress of the previous preshearing the effective stress paths are rendered less contractant, in triaxial extension even dilatant, following afterwards a more contractant path. However, the slope of the path without preloading at $p'_0 = p'_{0,2}$ is not recovered even after reaching the reversal point of the first loading step, indicating a partial alteration of the inherent anisotropy. Here it appears that the preloading path is retraced like an attractor. Finally, the shear strength is higher after a large preshearing (near the CSL), while the sample stiffness is increased in the preloading direction.

4 Constitutive description

In [36, 42, 60, 64] it has been shown that the inherent anisotropy of fine-grained soils can be described in constitutive models by the cross-isotropic elastic stiffness proposed by [17] and has been incorporated to several constitutive models (e.g. [13, 14, 26, 66]).

Two constitutive models are herein inspected using the presented experiments. First, the rather simple and well-known elastoplastic modified Cam Clay (MCC) model described in [5, 50] is considered. Besides, the anisotropic visco-hypoplastic model (AVHP) by [41] is used. This

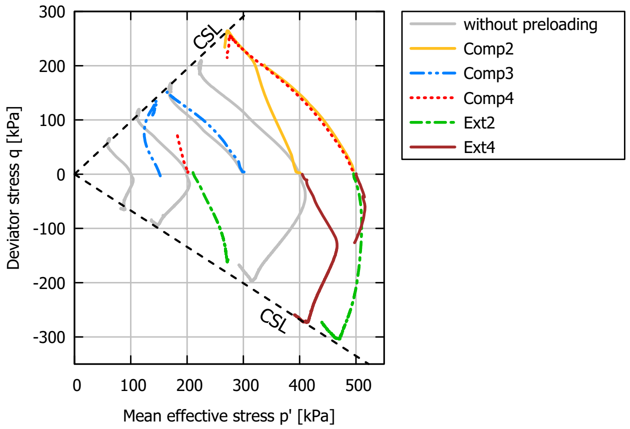

Fig. 11 Overview of all presented triaxial effective stress $p' - q$ paths on kaolin samples cut out in vertical direction with preshearing (coloured) and without preshearing (grey)

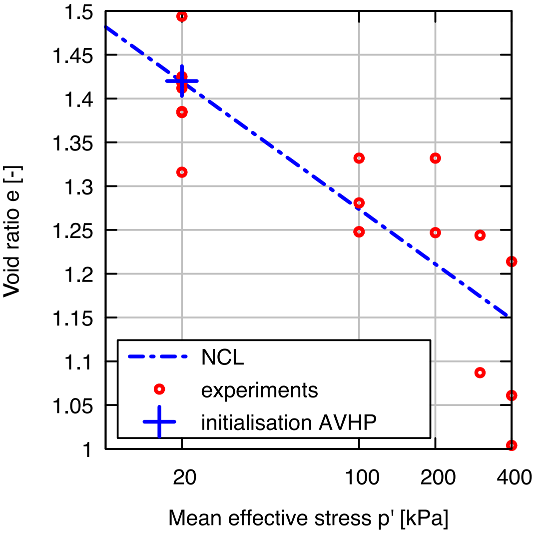

Fig. 12 Void ratios of experiments and initialisation of the simulations

model has been extended in the following by a cross-isotropic elastic stiffness as explained in [65] to capture the inherent anisotropy of the kaolin used in this work. The verification of the models considering the presented experiments follows after a short summary of the equations defining the reference AVHP model along with the introduction of the enhancement for inherent anisotropy.

4.1 Reference model - anisotropic visco-hypoplasticity by [41]

This model, in the sequel referred to either as reference model or as AVHP model was shown to reproduce well the description of creep, relaxation and rate dependence, improve the response to cyclic loading by a new strain rate $\dot{\boldsymbol{\varepsilon}}^{hp}$ and, of course, provide an induced anisotropic enhancement which can be observed in the response to triaxial (or biaxial) compression and extension paths after anisotropic K_0 consolidation. Hence the model introduces the induced anisotropy by a new state variable $\boldsymbol{\Omega}$. Herein the constitutive equations will be described briefly and for further details the attentive reader is referred to the reference work by [41].

The model interrelates the stress rate with three strain rates through a hypoelastic barotropic stiffness

$$\dot{\boldsymbol{\sigma}}' = \mathsf{E}^{iso} : \left(\dot{\boldsymbol{\varepsilon}} - \dot{\boldsymbol{\varepsilon}}^{vis} - \dot{\boldsymbol{\varepsilon}}^{hp}\right) \tag{1}$$

with the visco-plastic $\dot{\boldsymbol{\varepsilon}}^{vis}$ and the hypoplastic $\dot{\boldsymbol{\varepsilon}}^{hp}$ strain rate

$$\dot{\boldsymbol{\varepsilon}}^{vis} = D_r \ \mathrm{OCR}^{-1/I_v}\,\mathbf{m}, \quad \dot{\boldsymbol{\varepsilon}}^{hp} = C_1\mathbf{m}\|\dot{\boldsymbol{\varepsilon}}\| \tag{2}$$

and the flow rule

$$\mathbf{m} = \frac{\partial F_+(\boldsymbol{\sigma}', \boldsymbol{\Omega}, p'_{B+})}{\partial \boldsymbol{\sigma}}. \tag{3}$$

D_r as the reference creep rate as well as the viscosity index I_v are material parameters, whereby the latter determines the intensity of creep. C_1 is a material parameter, which is introduced aiming an improvement of the description of initial secant stiffness effects, hence cyclic loading.

The induced anisotropy is included through the inclined preloading surface $F(\boldsymbol{\sigma}', \boldsymbol{\Omega}, p'_B)$

$$F(\boldsymbol{\sigma}', \boldsymbol{\Omega}, p'_B) = M^2p^2 - 3Mp\boldsymbol{\sigma}'^* : \boldsymbol{\Omega} + \frac{3}{2}\boldsymbol{\sigma}'^* : \boldsymbol{\sigma}'^* \\ + M^2p'\,p'_B\left[\frac{3}{2}\boldsymbol{\Omega} : \boldsymbol{\Omega} - 1\right] = 0 \tag{4}$$

with the preloading stress $\boldsymbol{\sigma}_B = p'_B(-\boldsymbol{1} + \boldsymbol{\Omega}M_{\boldsymbol{\Omega}})$. p'_{B+} is calculated from Eq. 4 using the same inclination $\boldsymbol{\Omega}$, but passing through the current stress $\boldsymbol{\sigma}'$ rather than through $\boldsymbol{\sigma}_B$ which corresponds to the current void ratio (see Fig. 25a). In this sense, the overconsolidation ratio reads OCR$= p'_B/p'_{B+}$. The slope of the critical state in triaxial conditions $M = f(\theta)$ is dependent on the Lode angle \theta and obeys the Matsuoka-Nakai criterion and obeys the Matsuoka-Nakai criterion

$$f_{M-N} = \ \mathrm{tr}\ \boldsymbol{\sigma}' \ \ \mathrm{tr}\ (\boldsymbol{\sigma}'^{-1}) - \frac{9 - \sin^2\varphi_c}{1 - \sin^2\varphi_c} \tag{5}$$

with the critical friction angle φ_c.

The evolution of the state variables $\boldsymbol{\Omega}$ and p'_B are formulated in terms of the total strain rate $\dot{\boldsymbol{\varepsilon}}$ as follows

$$\dot{\boldsymbol{\Omega}} = C_2\left(C_3(-\hat{\boldsymbol{\sigma}}'^*) - \frac{1}{3}M\boldsymbol{\Omega}\right)\ \mathrm{OCR}^{-1/I_v} \cdot \langle\ \mathrm{tr}\ \dot{\boldsymbol{\varepsilon}}\rangle\langle-\ \mathrm{tr}\ \mathbf{m}\rangle \tag{6}$$

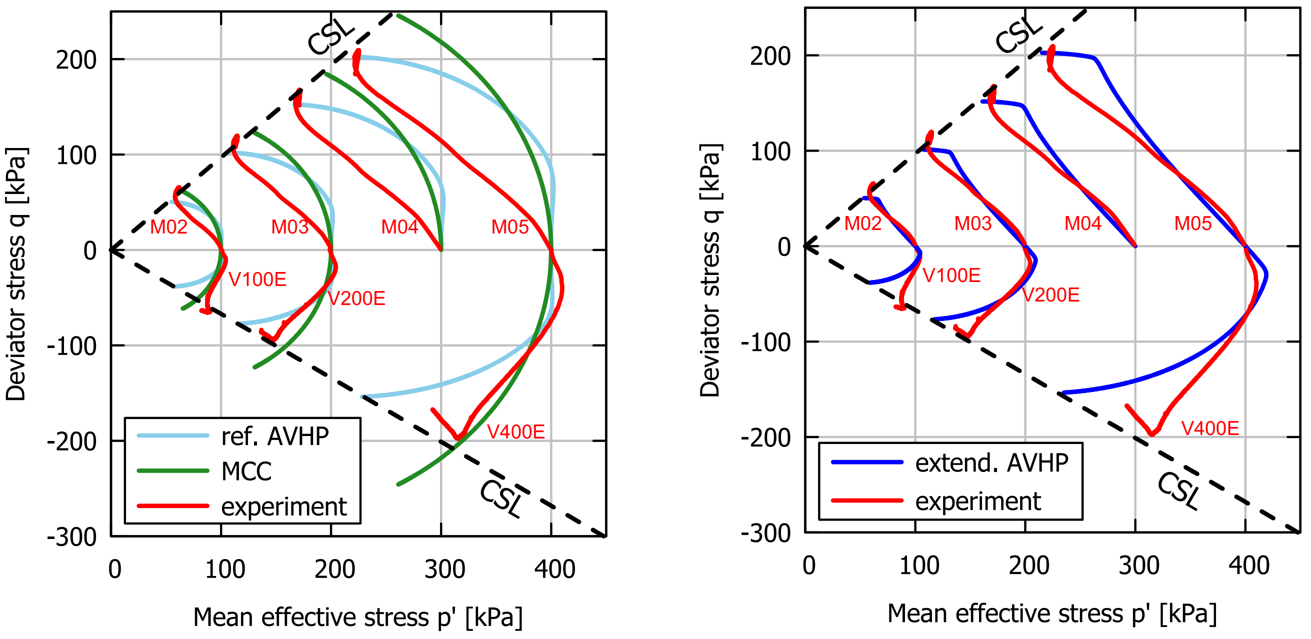

(a) MCC and reference AVHP model vs. experiment (b) Extended AVHP model vs. experiment

Fig. 13 Simulations of monotonic triaxial tests on kaolin samples cut out in vertical direction: $p' - q$ and $e - p$ space

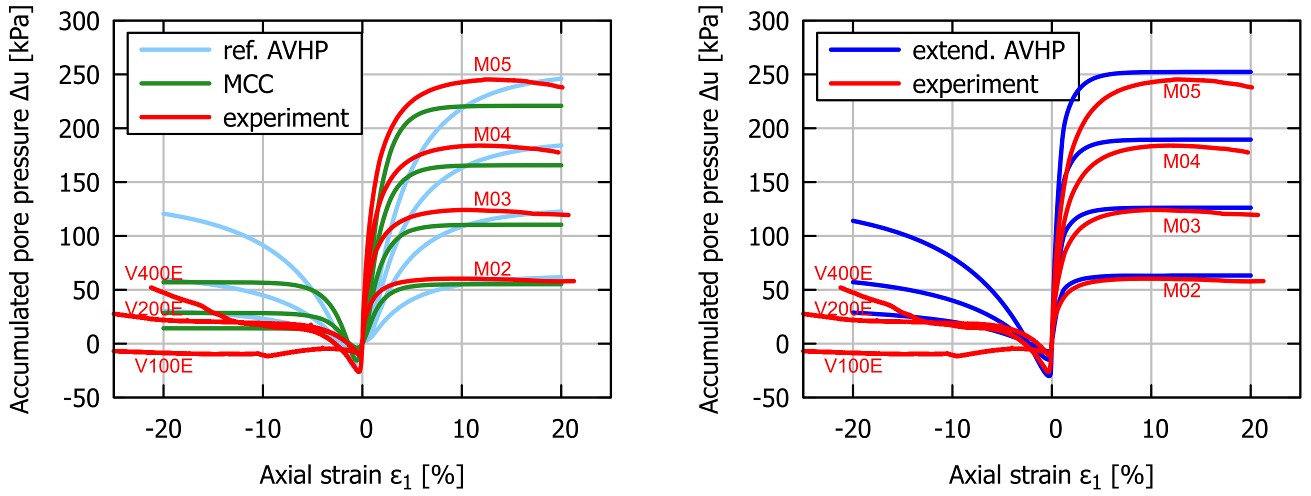

(a) MCC and reference AVHP model vs. experiment (b) Extended AVHP model vs. experiment

Fig. 14 Simulations of monotonic triaxial tests on kaolin samples cut out in vertical direction: excess pore water pressure Δu versus axial strain ε_1 space

$$\dot{p}'_B = -\frac{p'_B}{\lambda}\ \mathrm{tr}\ \dot{\boldsymbol{\varepsilon}} \tag{7}$$

whereby the preconsolidation pressure p'_B satisfies the equation of the isotropic reference isotach

$$\ln\left(\frac{1+e}{1+e_0}\right) = -\lambda\ \ln\left(\frac{p'_B}{p'_{B0}}\right). \tag{8}$$

C_2 and C_3 are material parameters controlling the evolution rate of the preconsolidation stress.

4.2 Extension for inherent anisotropy

In order to capture the inherent anisotropy of sedimentary fine-grained soils manifested in form of initial secant stiffness anisotropy the (hypo)elastic stiffness tensor is

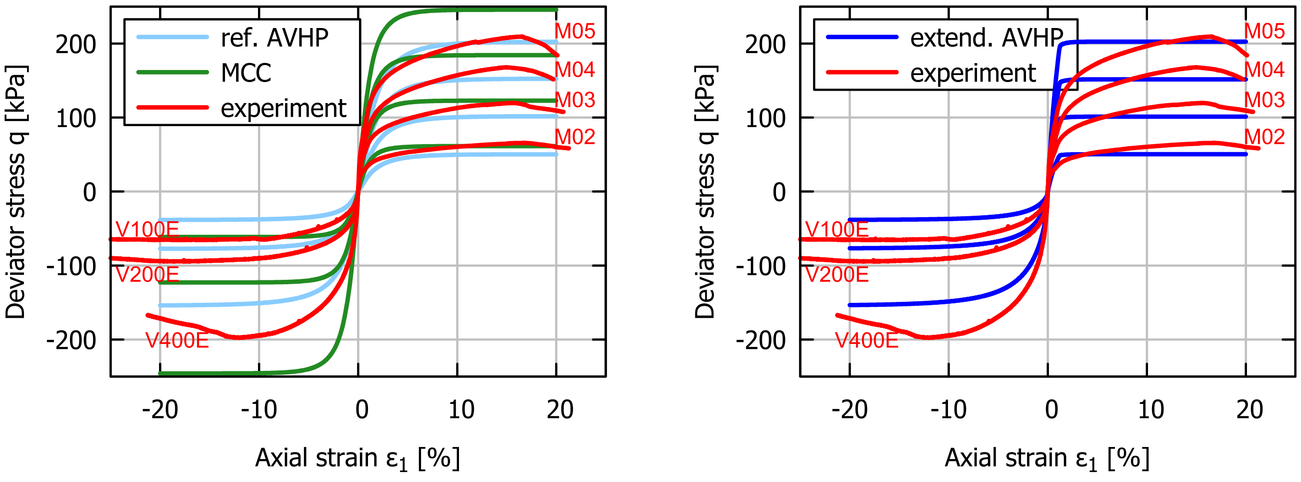

(a) MCC and reference AVHP model vs. experiment

(b) Extended AVHP model vs. experiment

Fig. 15 Simulations of monotonic triaxial tests on kaolin samples cut out in vertical direction: deviator stress q versus axial strain ε_1 space

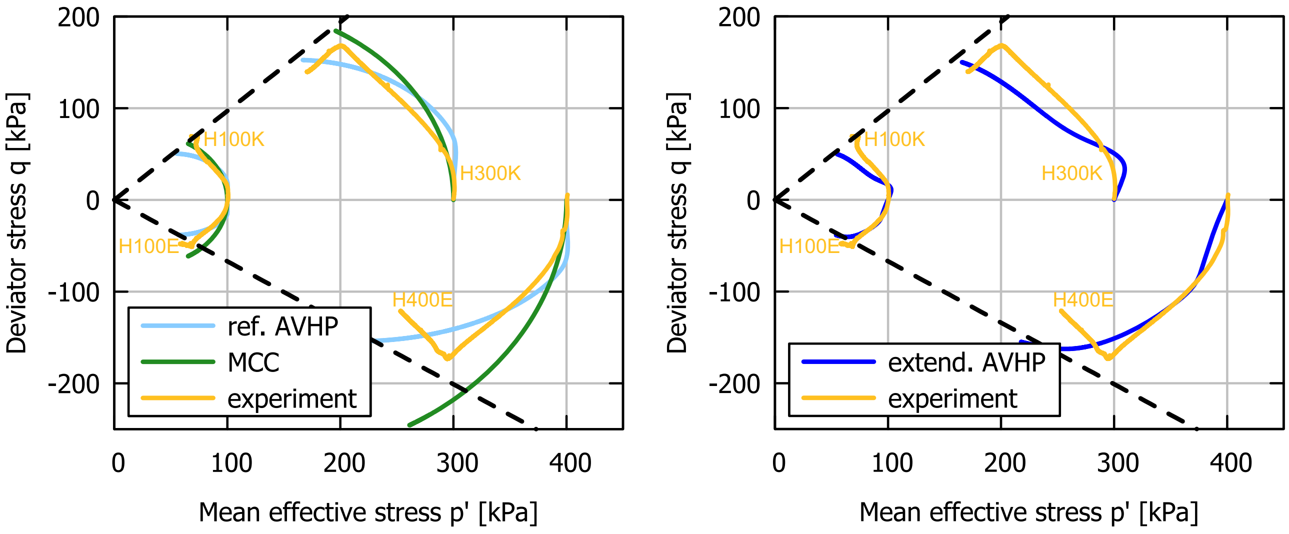

(a) MCC and reference AVHP model vs. experiment

(b) Extended AVHP model vs. experiment

Fig. 16 Simulations of monotonic triaxial tests on kaolin samples cut out in horizontal direction: $p' - q$ space

scaled to a cross-isotropic tensor using the manipulations developed in [17, 36, 42, 66]. Following the work of [17] the two isotropic elastic parameters $E = E_v$ and $\nu = \nu_h$ are supplemented in [66] by only one anisotropy material parameter, named anisotropic coefficient α

$$\alpha = \frac{G_h}{G_v} = \left(\frac{E_h}{E_v}\right)^{1/2} = \nu_h/\nu_{vh}. \tag{9}$$

In [42], besides α, the parameter β is introduced, satisfying the following relationship

$$\alpha = \frac{G_h}{G_v} = \left(\frac{E_h}{E_v}\right)^{\beta/2} = (\nu_h/\nu_{vh})^{\beta} = (\nu_{hv}/\nu_h)^{\beta} \tag{10}$$

[36] have reviewed existing experimental data in the literature pointing out that the value of the anisotropy exponent β is difficult to evaluate and recommended thereby an average value of $\beta = 1.6$ for practical applications. Here, the approach proposed in [42], is used; hence the parameter β is adjusted to fit the experimental database. The isotropic elastic stiffness is scaled using the anisotropy tensor Q from [42]

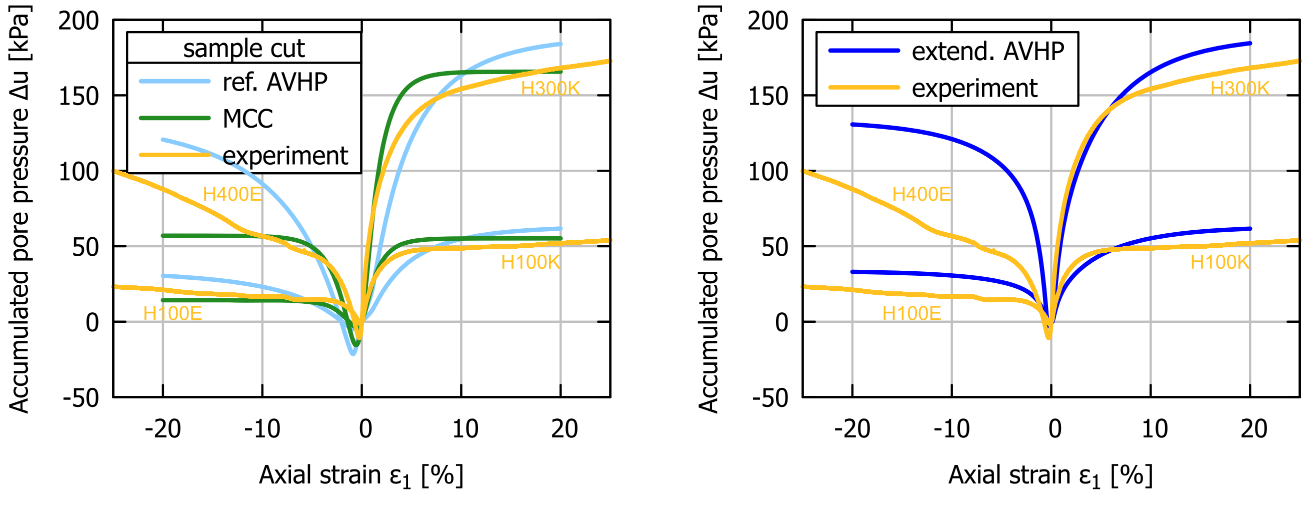

(a) MCC and reference AVHP model vs. experiment

(b) Extended AVHP model vs. experiment

Fig. 17 Simulations of monotonic triaxial tests on kaolin samples cut out in horizontal direction: excess pore water pressure Δu versus axial strain ε_1 space

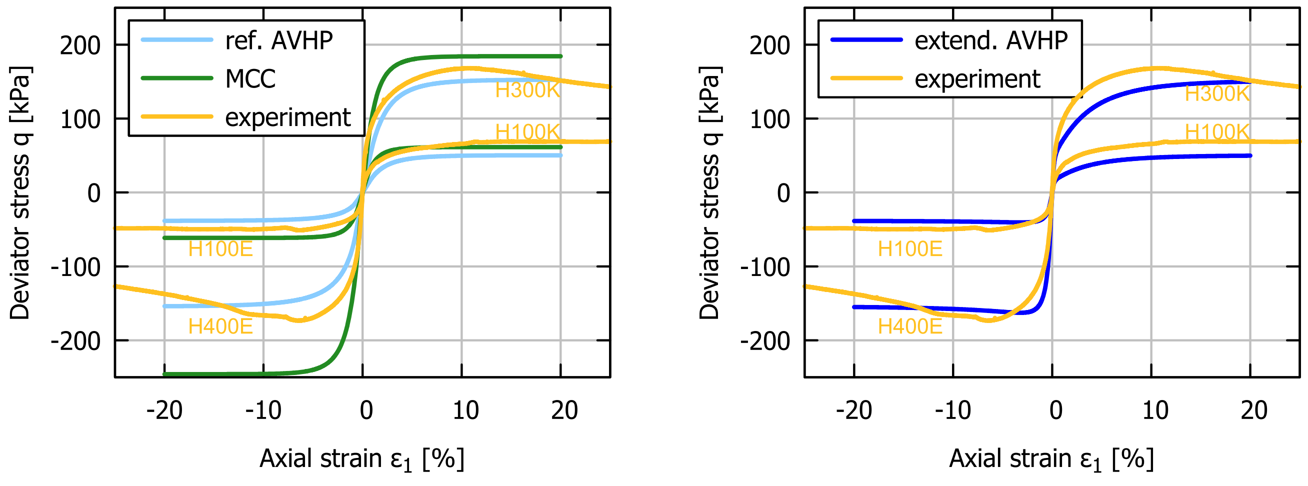

(a) MCC and reference AVHP model vs. experiment

(b) Extended AVHP model vs. experiment

Fig. 18 Simulations of monotonic triaxial tests on kaolin samples cut out in horizontal direction: deviator stress q versus axial strain ε_1 space

$$\mathsf{E} = \mathsf{Q}^T : \mathsf{E}^{iso} : \mathsf{Q} \tag{11}$$

$$Q_{ijkl} = \mu_{ik}\mu_{jl} + cI_{ijkl}, \quad \mu_{ik} = a\delta_{ik} + b\, m_i m_k \tag{12}$$

with a, b, c being functions of the constants α and β

$$a = -\sqrt{\alpha^{2\beta}\left((\sqrt{\alpha}-1)^2 + 2\alpha^{\beta-1/2} + (\alpha-3)\alpha^{\beta}\right)/d} \tag{13}$$

$$b = -\alpha^{-\beta} a\left(\alpha + \sqrt{\alpha} - \alpha^{\beta+1/2} + \alpha^{\beta+1} - 2\alpha^{\beta}\right)/(\alpha-1) \tag{14}$$

$$c = \alpha^{\beta-1/2}\left(\alpha - \alpha^{\beta}\right)\left(\sqrt{\alpha} + \alpha^{\beta+1/2} + 2\alpha^{\beta}\right)/d \tag{15}$$

and $d = \alpha + (\alpha - 4)\alpha^{2\beta} + 2\alpha^{\beta+1}$.

Calibration of additional material parameters

Ideally, ν_h is calibrated by direct measurements of shear and compressional wave velocities (e.g., bender elements or ultrasonic testing). If such data are not available, α and ν_h can be calibrated jointly from the measured inclination

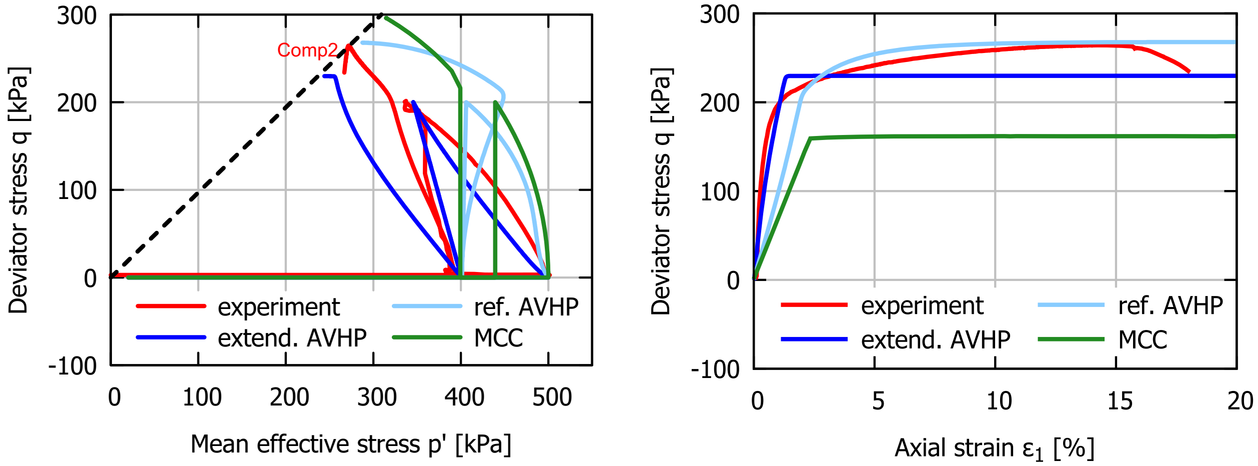

(a) Effective stress paths in the p'-q plane

(b) Deviator stress q vs. axial strain ε_1 in the second shearing step until failure

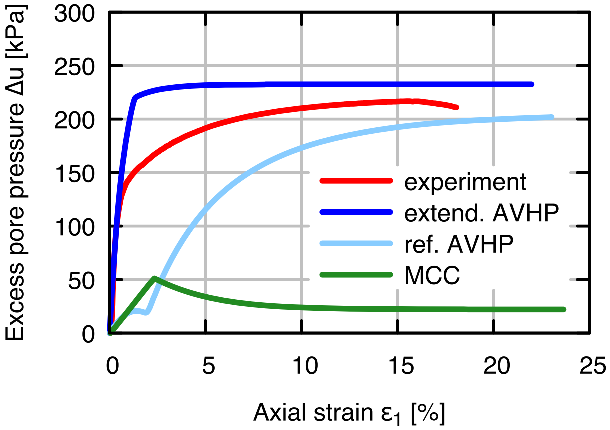

(c) Excess pore pressure Δu in the second shearing step until failure

Fig. 19 Simulations with MCC, reference AVHP and extended AVHP models compared to the test Comp2

of the effective stress path $\Delta p'/\Delta q$ in undrained triaxial tests, following [62, 66]. A consistent parameter pair is obtained by varying α and identifying the corresponding ν_h that reproduces the experimental slopes, while keeping ν_h within typical ranges for silts and clays.

4.3 Inspection of the models

This section evaluates the performance of three constitutive models: the elastoplastic MCC model, the hypoplastic AVHP model, and an extended version of the AVHP model introduced in Sect. 4.2 (referred to hereafter as the extended or in the figures extend. AVHP model). The focus lies on assessing the influence of initial secant stiffness anisotropy by comparing the original AVHP model with its extended counterpart.

The widely established MCC model requires solely 4 material parameters listed in Table 4. Besides these 4 parameters, the reference AVHP model requires 6 additional parameters while the extended AVHP model needs two parameters in addition, which are listed in Table 5. The calibration of the common parameters comprising the compression λ and swelling κ index has been done using the oedometric test with loading and unloading from [74], the critical friction angle φ_c has been determined by connecting the critical state points in the effective stress space, which render a line with the slope $M_c = 6 \cdot \sin(\varphi_c)/(3 - \sin(\varphi_c))$. The Poisson's ratio ν is required for the MCC model and was fitted using the $q - \varepsilon_1$ relationships of normally consolidated samples in the area of small-strains. Other parameters of the reference AVHP model comprising the reference void ratio e_{100} at $p'_{ref} =$ 100 kPa, the reference creep rate D_r, viscosity index I_v, parameter for cyclic loading C_1, factor for the evolution of induced anisotropy C_2 and for limiting that evolution C_3

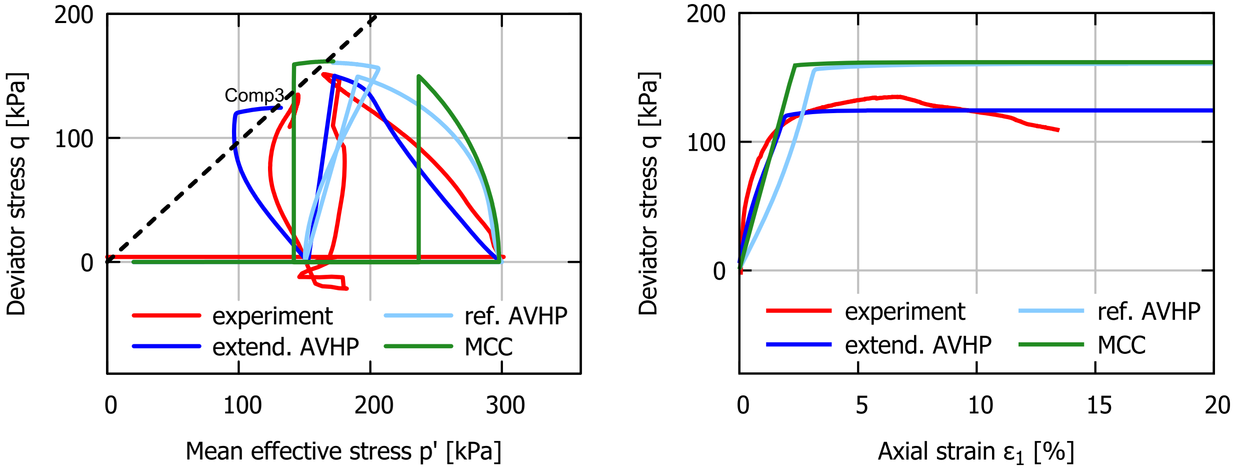

(a) Effective stress paths in the p'-q plane

(b) Deviator stress q vs. axial strain ε_1 in the second shearing step until failure

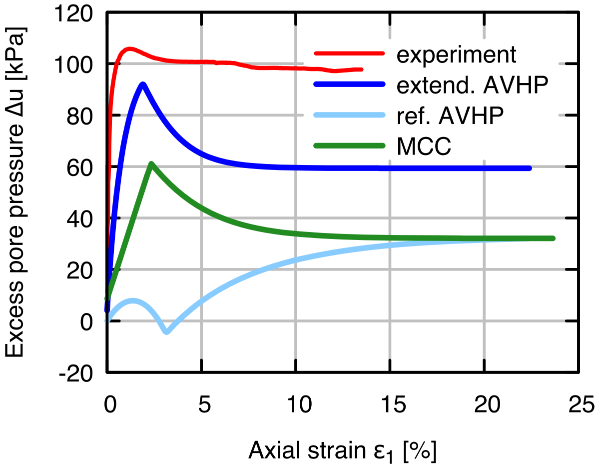

(c) Excess pore pressure Δu in the second shearing step until failure

Fig. 20 Simulations with MCC, reference AVHP and extended AVHP models compared to the test Comp3

are taken from the calibration presented in the diploma thesis of [56][1] and are detailed in [41] considering the experimental database for kaolin presented in [74]. In this sense, the performance of the model can be actually validated by simulating the tests with more complicated stress paths represented in Sect. 3.3. The additional parameters of the extended AVHP model regarding initial secant stiffness anisotropy α and β are calibrated using the experiments presented in Sect. 3.2. The advantage of the cross-isotropic elastic stiffness proposed by [17, 36, 42, 64] for describing the inherent anisotropy of cohesive soils is then verified by comparing simulations of the tests presented in Sect. 3.3 with MCC (isotropic elastic stiffness), reference AVHP model (isotropic hypoelastic stiffness) and the extended AVHP model (cross-isotropic hypoelastic stiffness).

The void ratios measured in the laboratory exhibited considerable scatter, which is shown in Fig. 12. In all simulations, the void ratio has been initialised following Eq. 8. The initial structural tensor $\mathbf{\Omega}_0 = \boldsymbol{0}$ vanishes due to initial isotropic consolidation state of all samples. The initial preloading stress $p'_{B,0}$ of the AVHP model as well as the initial preconsolidation pressure $p'_{c,0}$ of the MCC model are set equal to the initial mean effective stress $p'_{B,0} = p'_{c,0} = p'_0$ and all subsequent (pre)loading stages are modelled. The initial void ratio $e = 1.42$ and initial mean effective stress $p' = 20\,\text{kPa}$ were used for both the AVHP reference model and the extended AVHP model, see Fig. 12. The isotropic consolidation stages were simulated to establish the respective initial mean effective stresses

---

[1] The authors will make the diploma thesis available upon reasonable request.

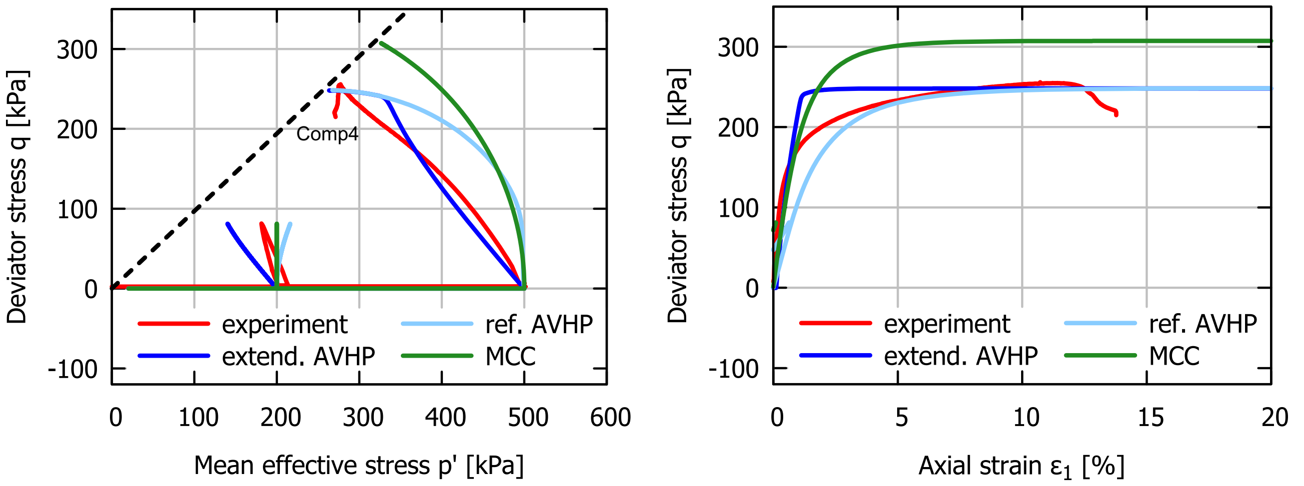

(a) Effective stress paths in the p'-q plane

(b) Deviator stress q vs. axial strain ε_1 in the second shearing step until failure

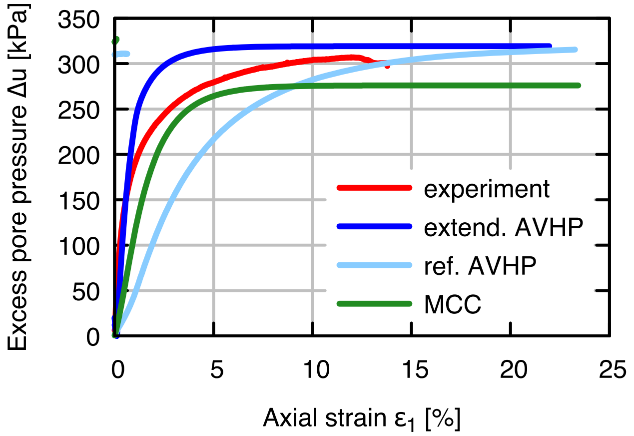

(c) Excess pore pressure Δu in the second shearing step until failure

Fig. 21 Simulations with MCC, reference AVHP and extended AVHP models compared to the test Comp4

before shearing, allowing for the evolution of $\boldsymbol{\Omega}$ during consolidation. In contrast, for the MCC model, initialisation was performed immediately after the first consolidation stage, as it does not account for the evolution of a structure tensor.

4.3.1 Monotonic triaxial tests

Figures 13a, 14a and 15a present the simulations of triaxial tests performed on samples cut out in vertical direction with the MCC model and the reference AVHP model in $p' - q$, $q - \varepsilon_1$ and excess pore water pressure Δu versus axial strain ε_1 space, respectively. It is apparent that the MCC model exceeds the shear strength in both triaxial compression and extension, achieving the same slope of the critical state line (CSL) in both directions, contrary to the experimental observations. The reference AVHP model reaches the accurate slope of the CSL (illustrated with dotted black line in Fig. 13) and realistic shear strength in both triaxial compression and extension (see Fig. 15a), but exceeds the mean effective stress until the CSL is attained. The cause of this lies in the underestimation of the pore water pressure build-up as seen in Fig. 14a for both the MCC and the reference AVHP model. Herein is where the initial secant stiffness anisotropy, introduced by scaling the isotropic hypoelastic stiffness tensor in the reference AVHP model to a cross-isotropic tensor in the extended AVHP model, takes effect. As shown in Fig. 13b, the slope of the effective stress path changes in the extended AVHP model corresponding to the one observed in the experiment and thus, in Fig. 14b the excess pore water pressure is reproduced realistically. The initial dilatancy is quantitatively well reproduced with the extended model, while it is

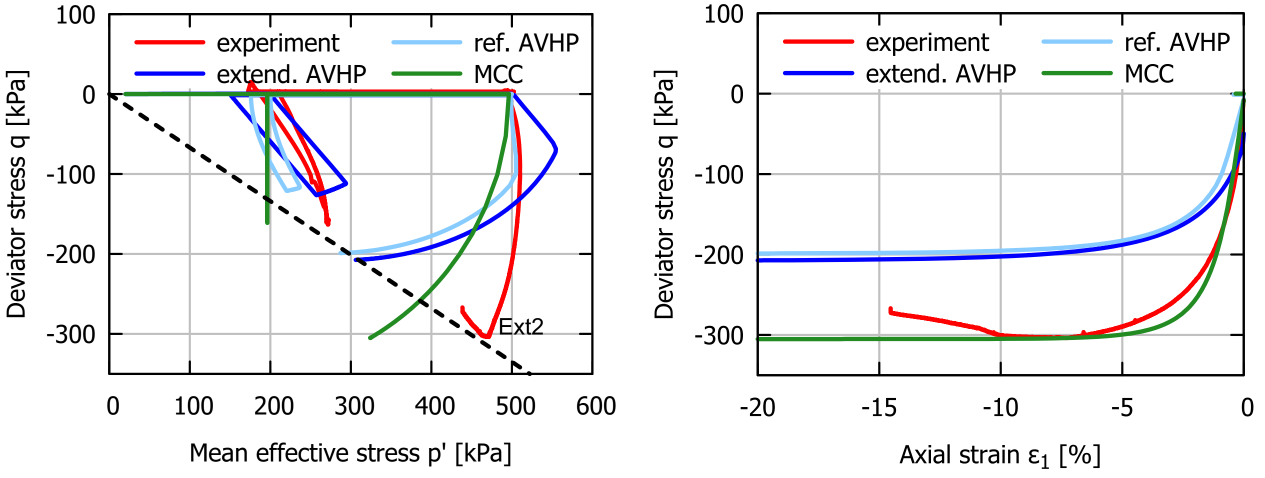

(a) Effective stress paths in the p'-q plane

(b) Deviator stress q vs. axial strain ε_1 in the second shearing step until failure

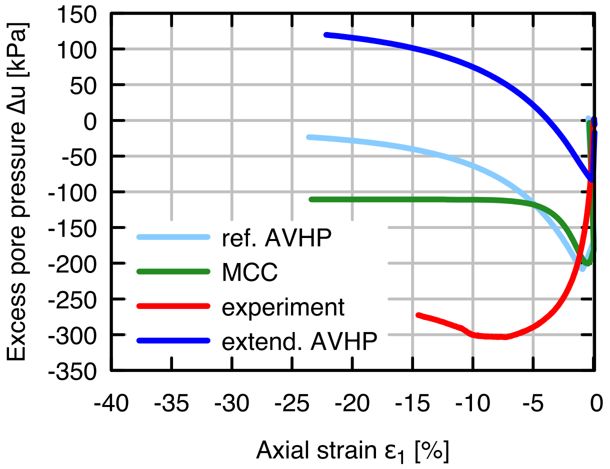

(c) Excess pore pressure Δu in the second shearing step until failure

Fig. 22 Simulations with MCC, reference AVHP and extended AVHP models compared to the test Ext2

underestimated with the models in Fig. 14a. Some small discrepancies are observed in triaxial extension, where the preloading surface is probably too thin and thus the plasticity generates a too fast and too high pore water pressure build-up. It was not possible to adjust it more realistically by varying the parameters C_2 and C_3. While in triaxial compression the incorporation of a transversal isotropic elastic stiffness tensor renders a good reproduction of the experimental observations, in triaxial extension it still lacks on reaching the accurate shear strength due to an overestimation of contractancy. This occurrence points out to a need of a more non-uniform preloading surface differentiating between triaxial extension and compression, especially in the rate of evolution of the structural tensor $\mathbf{\Omega}$ as pointed out also in [63]. Furthermore, the use of a non-associated plastic flow rule with a physically realistic plastic potential function could provide greater flexibility for MCC in reproducing the pore pressure evolution and yield more accurate predictions of the Δu–ε_1 relationship. In the present study, however, an associated flow rule was adopted to ensure consistency with the established framework and facilitate direct comparison between models.

Nevertheless, it can be concluded that the inherent anisotropy of soft soils described by the anisotropy of initial secant stiffness is indispensable in problems with fast undrained loading where the build-up of pore water pressure plays a decisive role. Accordingly, it can be seen from Fig. 16a that the MCC and the reference AVHP model reproduce the elastic stiffness of the horizontally cut out specimens more appropriately than that of the vertical specimens (compare Fig. 13). There is no significant difference between the simulations of the reference AVHP

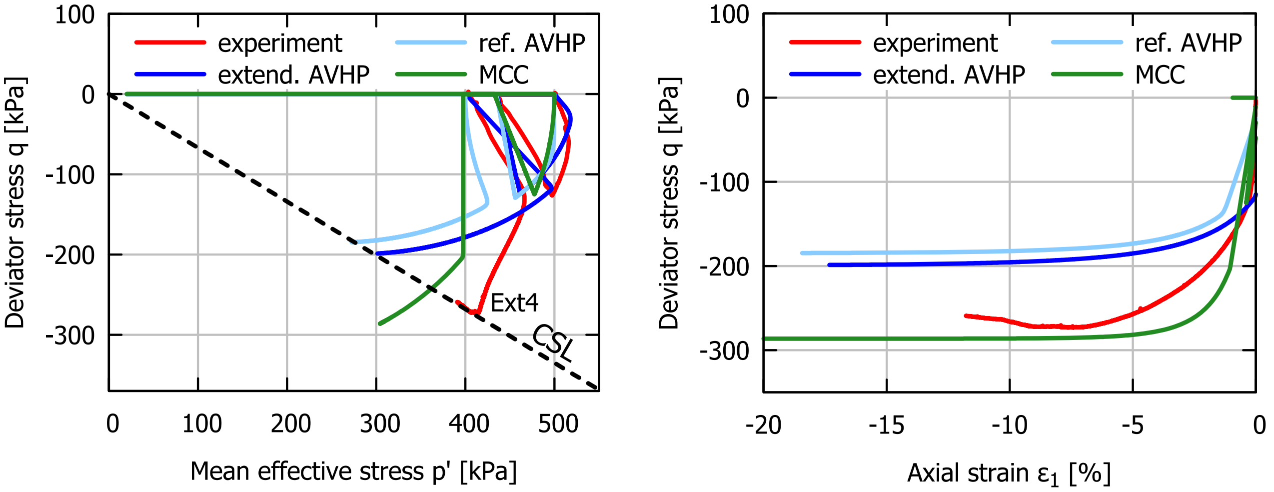

(a) Effective stress paths in the p'-q plane

(b) Deviator stress q vs. axial strain ε_1 in the second shearing step until failure

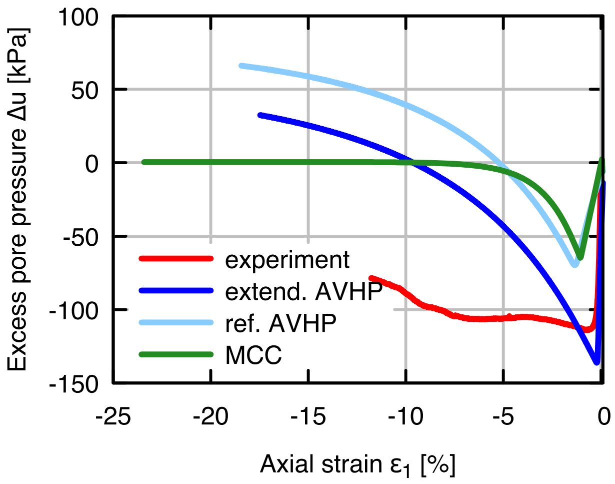

(c) Excess pore pressure Δu in the second shearing step until failure

Fig. 23 Simulations with MCC, reference AVHP and extended AVHP models compared to the test Ext4

and the extended AVHP model here (Fig. 16b). The corresponding excess pore water pressures for horizontally cut samples can be found in Fig. 17. The overestimation of the shear strength through the MCC model is for horizontal samples mainly observed at higher initial pressures with subsequent shear in triaxial extension, see Figs. 16a and 18a.

4.3.2 Triaxial tests with different preshearing history

In this section all considered models are used for simulations of the tests with preshearing history. In this test series, all samples were cut out vertically.

Figure 19a shows the $p' - q$ space of the test Comp2, whereby as described before the initial secant stiffness anisotropy leads to an inclined effective stress path to the upper left of the $p' - q$ space when subjected to loading in triaxial compression. This tendency can be described only with the extended AVHP model, implying a better agreement of the subsequent undrained shearing until failure in compression. More pronounced is this behaviour in Fig. 20 whereby the larger preshearing took place until near the CSL. In both experiments can be observed an overestimation of the shear strength by the MCC and the reference AVHP model. Furthermore, it is evident that the inherent anisotropy is not altered even with a preshearing up to the CSL, which is in accordance with its description in terms of initial secant stiffness anisotropy or cross-isotropic elasticity. The resulting stress path at second shearing is a combination of an overconsolidated path and the stress

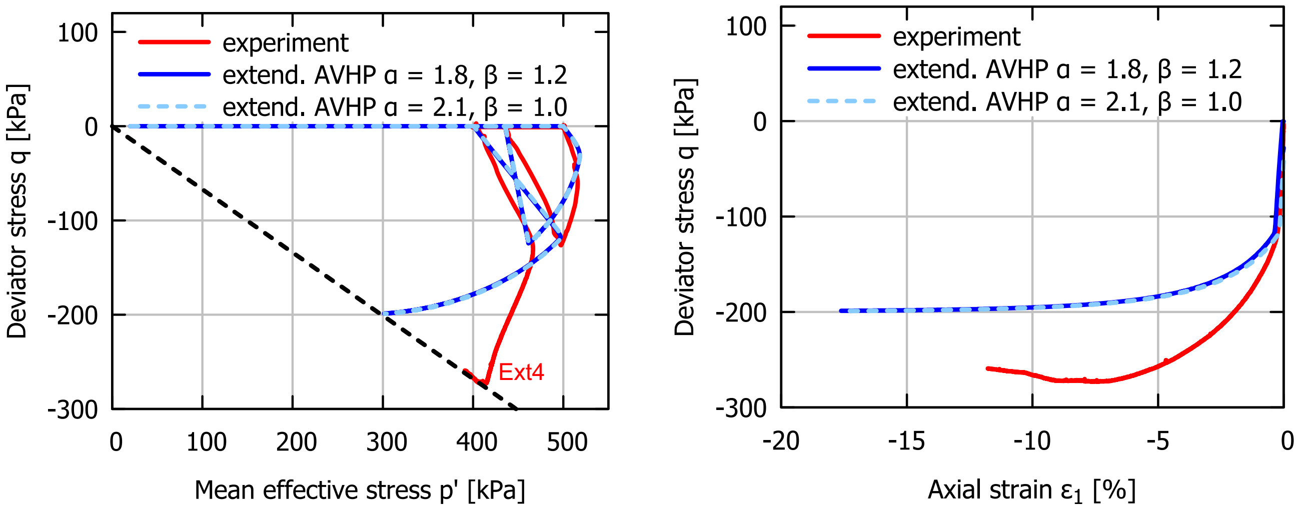

(a) Effective stress paths in the p'-q plane (b) Deviator stress q vs. axial strain ε_1 in the second shearing step until failure

Fig. 24 Simulations with the extended AVHP model of the test Ext4 with different values of parameters α and β

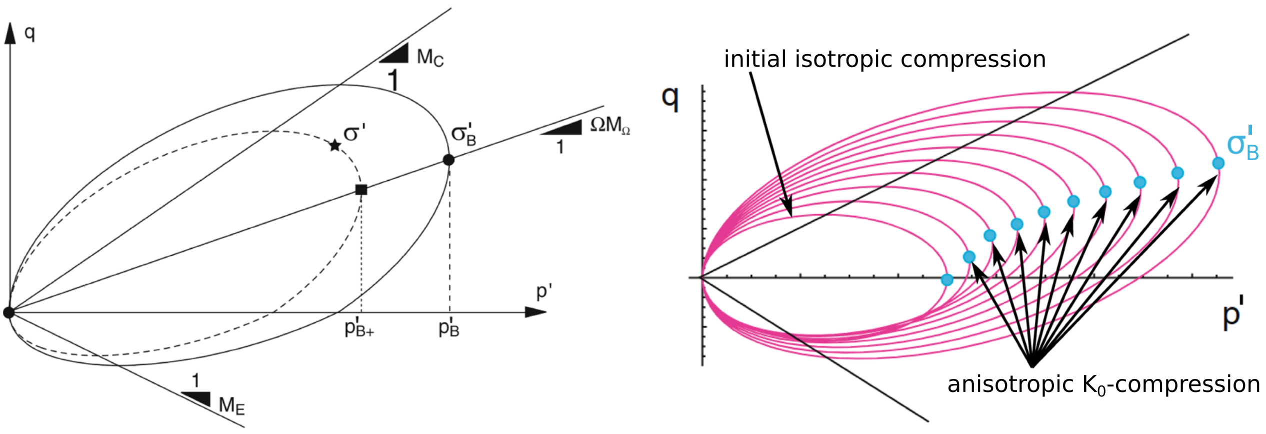

(a) Visualization of the preloading surface in the p'-q-space with preloading pressure p'_B and the definition of $p_B^{+\prime}$, modified from [42]. (b) Preloading surface for initial isotropic compression and following anisotropic K_0-compression, modified from [42]

Fig. 25 Preloading surface of the AVHP model and its evolution

path inclined by the inherent anisotropy, which can be reproduced well by the extended AVHP model. However, in test Comp3 (Fig. 20b), the model simulation overestimates the shear strength during the second shearing. This overestimation occurs because the model predicts an excessive increase in the effective stress path inclination, driven by the rise in the overconsolidation ratio .

Similar observations are presented in Fig. 21, whereby the sample was first sheared by a small deviator stress of $q \approx 95$ kPa in compression at $p'_{0,1} = 200$ kPa with an initial overconsolidation ratio of $\mathrm{OCR}_1 = 2.5$. Even if less, the effective stress path is still inclined to the upper left and can be partially reproduced by the extended AVHP model. Comparing the corresponding experiment in Fig. 13b at $p'_0 = 200$ kPa without preloading, it can be concluded that isotropic preloading leads to a reduction of contractancy under triaxial shearing. This cannot be reproduced only with the initial secant stiffness anisotropy. Therefore, different approaches for ageing [22] or fabric change [7, 35, 45, 66] are used in the literature. As expected, the MCC model shows an elastic response (vertical stress path) while the reference AVHP model produces a dilatant stress path contrary to experimental observations.

The sample in Fig. 22 was first sheared in triaxial extension with a deviator stress of $q \approx -190$ kPa at $p'_{0,1} \approx 200$ kPa and $\mathrm{OCR1} = 2.5$ (the counterpart of Comp4 in Fig. 21), where the extended AVHP model accurately captured the observed dilatant behaviour. During the second shearing, which continued until failure in triaxial extension beginning from a normally consolidated state with $p_{0,2} = 500$ kPa, the pore water pressure build-up was overestimated by both AVHP models. In contrast, the MCC model better replicated the experimental results despite intersecting the critical state line (CSL). Due to the extensive preshearing of the sample, the resultant shear strength during subsequent loading in triaxial extension increased. Although the MCC model does not account for the influence of preloading, as observed in Figs. 19a, 20, 21, 22 and 23a, it overestimates the shear strength in triaxial extension, which leads to better alignment with the increased shear strength of the preloaded sample in Fig. 23b. On the other hand, although the introduced transverse isotropic elastic stiffness tensor improves the AVHP predictions for triaxial compression, it still fails to accurately predict the shear strength in triaxial extension, both in conventional undrained triaxial tests and tests with preshearing, due to an overestimation of contractancy. This issue highlights the need for a more non-uniform preloading surface that distinguishes between triaxial extension and compression, particularly by being wider in triaxial extension, which leads to a decay of plasticity. Specifically, the rate of evolution of the structural tensor $\boldsymbol{\Omega}$ should be revised to more accurately account for the anisotropy induced by preloading, as also emphasised in [63].

The last experiment Ext4 in Fig. 23 comprises loading in triaxial extension first at a normally consolidated state with $p'_{0,1} = 500$ kPa initially sheared with a deviator stress of $q \approx -125$ kPa. The second shearing began at $p'_{0,2} = 400$ kPa and $\mathrm{OCR}_{0,2} = 1.25$ (calculated neglecting the change in deviator stress). Again, the inclination of the effective stress path can be described well by the extended AVHP model, whereas the preloading surface seems to be too thin and thus plastic strains yield to a higher pore water pressure build-up compared to the experiment. The reference AVHP and the MCC model show the same downwards and approximately vertical inclination in the $p' - q$ space, hence absence of pore water pressure build-up. During the second loading in triaxial extension the effective stress path described by the extended AVHP model is too much inclined to the bottom right compared to the experiment, which, among other things, is due to a disappearing plasticity within the preloading surface. After the stress state lies on the preloading surface (kink in the stress path in Fig. 23a), the contractant plasticity is overestimated and now the stress path is inclined too much to the bottom left. Thus, the shear strength reached at the critical state is underestimated as can be observed in the $q - \varepsilon_1$ space in Fig. 23b as well. The reference AVHP model reproduces similar results, except that the tendency of the initial pore water pressure build-up in the first shearing is an opposite one to that in the experiment. Due to the underestimation of dilatancy in the second shearing the shear strength is rendered similar to the one with the extended model. Eventhough the MCC model shows zero pore water pressure build-up inside the yield surface and exceeds the critical state line in triaxial extension it reaches nearly the exact ultimate shear strength as the sample in the experiment.

Some comparative studies with variation of α and β indicated, that a decrease of the new parameter β can be compensated by an increase of the parameter α and vice versa. As an example, Fig. 24 shows that $\alpha = 2.1$ and $\beta = 1.0$ yield to the exactly same simulation results as the parameters listed in Table 5 ($\alpha = 1.8$, $\beta = 1.2$) at least for the here presented. If the experimental data base is scarce, the parameter β may thus be omitted, which has the same effect as if it takes the value $\beta = 1.0$.

4.3.3 Discussion: capabilities, advantages, and limitations of the AVHP framework

The evolution of the anisotropic tensor $\boldsymbol{\Omega}$ in the AVHP model, and consequently the size and inclination of the preloading surface, is illustrated in Fig. 25 for representative loading paths. The behaviour of the surface directly follows from the hardening law in Eq. 6 and the dependence of $\boldsymbol{\Omega}$ on contractant volumetric strain rate.

Drained isotropic consolidation/compression: During drained isotropic loading, the stress path remains on the isotropic reference isotach and no shear stresses develop. As a result, the anisotropic tensor remains zero, $\boldsymbol{\Omega} = \mathbf{0}$, and the preloading surface stays non-inclined. Its size increases solely with the increase in mean effective stress. This behaviour corresponds to the leftmost contour in Fig. 25b.

For the extended AVHP model, the elastic stiffness tangent may be specified as anisotropic (i.e., $\alpha \neq 0$), which provides a direct means of representing inherent anisotropy.

Undrained monotonic triaxial compression and extension: Undrained loading is isochoric, i.e. $\mathrm{tr}(\dot{\varepsilon}) = 0$. In the AVHP model, $\boldsymbol{\Omega}$ evolves only for contractant volumetric strain paths, while p_B changes only for non-isochoric conditions. Consequently, during undrained compression and extension, the preloading surface does not evolve. The absence of surface rotation under undrained monotonic shearing therefore limits the model's ability to reproduce the experimentally observed effects of undrained preloading in the present work.

Pre-sheared triaxial compression and pre-sheared triaxial extension: When drained anisotropic pre-shearing is applied before the main loading stage, the resulting non-isotropic and non-isochoric stress path activates the evolution of $\boldsymbol{\Omega}$. This leads to a progressive rotation of the preloading surface towards the direction of the principal deviatoric loading and, in the presence of contractant volumetric strain, to a simultaneous increase in its size. In Fig. 25b, this behaviour is shown by the transition from isotropic compression points (blue markers) to the rotated surfaces generated during K_0-type loading (pink contours). Drained pre-shearing therefore establishes a rotated initial surface for the subsequent triaxial compression or extension stage, in agreement with experimentally observed anisotropic stress paths [10, 12, 44, 52, 54, 61].

In the undrained preloading stages of the present experiments, the AVHP preloading surface remains unchanged because no volumetric strain is generated. As a result, only the isotropic (re)consolidation step contributes to the subsequent evolution of the preloading surface. Overall, Fig. 25 provides a compact visualisation of how the AVHP framework captures the induced anisotropy under different loading conditions through the evolution of $\boldsymbol{\Omega}$.

In contrast, in rotational kinematic hardening frameworks, such as for, e.g. [3, 38, 46, 47, 49, 76], inherent anisotropy is introduced through an initial rotation of the yield and plastic potential surfaces. This rotational mechanism becomes active only once plastic strain initiates and, in [4], is formulated solely for triaxial stress conditions. Purely elastic stiffness is not part of the rotational mechanism, although anisotropic elasticity may be incorporated in the underlying constitutive model - consistent with the extension introduced here for the AVHP framework.

Similarly, anisotropic critical state theory (ACST), such as for, e.g. [27, 29, 47, 51], introduces anisotropy through a fabric tensor representing the internal soil structure [24, 53, 77]. The tensor evolves under loading, can model both induced anisotropy and the erasure of inherent anisotropy under isotropic compression, and approaches an asymptotic value at the critical state. Its evolution is not restricted to contractant volumetric strain paths and remains inactive along proportional stress paths. Across both classes of models, inherent anisotropy is embedded by prescribing an initial fabric tensor, which influences the response once the stress state reaches the yield surface, whereas elastic loading remains isotropic unless an anisotropic elastic law is explicitly introduced. The anisotropic elastic extension proposed here for the AVHP framework could likewise be incorporated into ACST-based bounding-surface formulations to enhance their ability to represent inherent structural anisotropy.

5 Conclusion

This paper provides an extension and completion of the data base on kaolin from [74]. These experiments include monotonic undrained triaxial tests in both compression and extension of specimens cut out in horizontal and vertical directions. Furthermore, the impact on the inherent anisotropy of samples cut out in the vertical direction of different preloading paths was inspected. As observed in [74] the inherent anisotropy of this kaolin leads to a different inclination of the effective stress path due to the distinct pore water pressure build up during shearing. The shear strength of horizontal cut out samples subjected to triaxial compression is higher than that of vertical cut out samples. It has been discovered that the fabric effects are more pronounced in triaxial compression, while when subjected to triaxial extension the horizontal samples show a slightly lower shear strength compared to vertical ones.

The most recent attempts in literature to describe the inherent anisotropy of clays by the initial secant stiffness anisotropy in means of transversal isotropic elastic stiffness tensor was applied to the AVHP model (see Sect. 4.2). While in triaxial compression it reflects the experimental observations well, in triaxial extension it still lacks on reaching the accurate shear strength in both conventional undrained triaxial tests as well as tests with preshearing due to an overestimation of contractancy. This occurrence points out to a need of a more non-uniform preloading surface differentiating between triaxial extension and compression, especially in the rate of evolution of the structural tensor $\boldsymbol{\Omega}$ as pointed out also in [63]. Even though the MCC model requires only 4 parameters, it describes well the overall behaviour of kaolin under monotonic loading with some discrepancies in the shear strength as well as critical state in triaxial extension. More recent versions of MCC model could be used instead, implying again a higher number of parameters. Here the aim was to show the improvement in prediction ability by increasing the complexity of the model. Furthermore it has been discovered that an increase of the new parameter β can be compensated by a reduction of the parameter α, so that at least for practical applications with a limited number of experiments the parameter β may be omitted.

Acknowledgements Parts of this research were funded by German Research Council (DFG) in the framework of the project TA 1696/1-1 and WI 3180/9-1. The financial support by DFG is gratefully acknowledged herewith. The tests have been performed by the technician H. Borowski in the IBF soil mechanics laboratory.

Funding Open Access funding enabled and organized by Projekt DEAL. Parts of this research were funded by German Research Council (Deutsche Forschungsgemeinschaft, DFG) in the framework of the project TA 1696/1-1 and WI 3180/9-1 and 447999811.

Data availability The datasets generated and analysed during the current study are available from the corresponding author on reasonable request.

Declarations

Conflict of interest The authors declare no conflict of interest.

References

1. Addenbrooke TI, Potts DM, Puzrin AM (1997) The influence of pre-failure soil stiffness on the numerical analysis of tunnel construction. Géotechnique 47(3):693–712
2. Anantanasakul P, Yamamuro JA, Lade P (2012) Three-dimensional drained behavior of normally consolidated anisotropic kaolin clay. Soils Found 52(1):146–159
3. Anantanasakul P, Kaliakin VN (2025) Evolution of cross-anisotropic behavior of clay under 3d stress conditions. Acta Geotech 20(7):3291–3308
4. Anantanasakul P, Yamamuro JA, Kaliakin VN (2012) Stress–strain and strength characteristics of silt-clay transition soils. J Geotech Geoenviron Eng 138(10):1257–1265
5. Borja RI, Seung RL (1990) Cam Clay plasticity, part 1: implicit integration of elasto-plastic constitutive relations. Comput Methods Appl Mech Eng 78:49–72
6. Coelho BZ, Dijkstra J, Karstunen M (2021) Viscoplastic cyclic degradation model for soft natural soils. Comput Geotech 135:104176
7. Dafalias Y, Manzari M (2004) Simple plasticity sand model accounting for fabric change effects. J Eng Mech 130(6):622–634
8. DIN EN ISO. 17892-9:2018-07, Geotechnische Erkundung und Untersuchung_- Laborversuche an Bodenproben_- Teil_9: Konsolidierte triaxiale Kompressionsversuche an wassergesättigten Böden (ISO_17892-9:2018); Deutsche Fassung EN_ISO_17892-9:2018
9. Duncan JM, Seed HB (1966) Anisotropy and stress reorientation in clay. J Soil Mech Found Division 92(5):21–50
10. Duque J, Roháč J, Mašín D (2023) On the influence of drained cyclic preloadings on the cyclic behaviour of zbraslav sand. Soil Dyn Earthq Eng 165:107666
11. Duque J, Rohac J, Mašín D, Najser J (2022) Experimental investigation on kaolin under monotonic and cyclic loading: inspection of undrained miner's rule and drained cyclic preloading. Acta Geotech 17:4953–4975
12. Duque J, Tafili M, Mašín D (2023) On the influence of cyclic preloadings on the liquefaction resistance of sands: a numerical study. Soil Dyn Earthq Eng 172:108025
13. Duque J, Tafili M, Seidalinov G, Mašín D, Fuentes W (2022) Inspection of four advanced constitutive models for fine-grained soils under monotonic and cyclic loading. Acta Geotech 17:4395–4418
14. Fuentes W, Mašín D, Duque J (2020) Constitutive model for monotonic and cyclic loading on anisotropic clays. Géotechnique 71(8):1–17
15. Ganal A, Reul O, Tafili M (2024) Visko-hypoplastisches materialmodell für tertiäre böden in frankfurt am main. *geotechnik*, 47(2):84–97
16. Gehring S, Knittel L, Tafili M (2021) Von der Hyperelastizität feinkörniger Böden zum Bodenverhalten unter zyklischer Beanspruchung. In *Fachsektionstage Geotechnik, 3. Bodenmechanik-Tagung*. Deutsche Gesellschaft für Geotechnik e.V
17. Graham J, Houlsby GT (1983) Anisotropic elasticity of a natural clay. Géotechnique 33(2):165–180
18. Grandas-Tavera Carlos E, Merita Tafili (2025) Simplified numerical simulation of vibrocompaction in sand. Transp Geotech 50:101406
19. Gunn M.J (1992) The prediction of surface settlement profiles due to tunnelling. In *Predictive soil mechanics: proceedings of the wroth memorial symposium held at St Catherine's college, Oxford,Thomas Telford Publishing, 27-29 July 1992*, pp 304–316
20. Hicher PY, Wahyudi H, Tessier D (2000) Microstructural analysis of inherent and induced anisotropy in clay. Mech Cohesive-frict Mater Int J Exp Modell Comput Mater Struct 5(5):341–371
21. Huang W-X, Wei W, Sun D-A, Sloan S (2006) A simple hypoplastic model for normally consolidated clay. Acta Geotech 1(1):15–27
22. Hyodo M, Hyde AFL, Yamamoto Y, Fujii T (1999) Cyclic shear strength of undisturbed and remoulded marine clays. Soils Found 39(2):45–58
23. Ignat R, Baker S, Karstunen M, Liedberg S, Larsson S (2020) Numerical analyses of an experimental excavation supported by panels of lime-cement columns. Comput Geotech 118:103296
24. Irani N, Salimi M, Golestaneh P, Tafili M, Wichtmann T, Lederer J (2024) Deep learning-based analysis of true triaxial dem simulations: role of fabric and particle aspect ratio. Comput Geotech 173:106529
25. Ishihara K, Okada S (1978) Effects of stress history on cyclic behavior of sand. Soils Found 18(4):31–45
26. Jerman J, Mašín D (2020) Hypoplastic and viscohypoplastic models for soft clays with strength anisotropy. Int J Numer Anal Meth Geomech 44(10):1396–1416
27. Jong Yong-Gwang, Ri Song-Chol (2025) An anisotropic critical state hypoplastic model considering the relation between fabric anisotropy variable and density function. *Mech Solids*, 1–11
28. Karstunen M, Koskinen M (2008) Plastic anisotropy of soft reconstituted clays. Can Geotech J 45(3):314–328
29. Kaviani-Hamedani F, Fakharian K, Lashkari A (2021) Bidirectional shear wave velocity measurements to track fabric anisotropy evolution of a crushed silica sand during shearing. J Geotech Geoenviron Eng 147(10):04021104
30. Kinner E.B (1973) Undrained bearing capacity of footing on clay. In *Proc. of the 8th Int. Conf. on SMFE, Moscow*, vol 1, pp 209–215
31. Knittel L, Tafili M, Tavera CG, Triantafyllidis T (2023) New perspectives on preshearing history in granular soils. Sci Rep 13(1):4576. https://doi.org/10.1038/s41598-023-31419-9
32. Knittel L, Wichtmann T, Niemunis A, Huber G, Espino E, Triantafyllidis Th (2020) Pure elastic stiffness of sand represented by response envelopes derived from cyclic triaxial tests with local strain measurements. Acta Geotechnica 15(8):2075–2088. https://doi.org/10.1007/s11440-019-00893-9
33. Kurukulasuriya LC, Oda M, Kazama H (1999) Anisotropy of undrained shear strength of an over-consolidated soil by triaxial and plane strain tests. Soils Found 39(1):21–29

34. Lai VQ, Shiau J, Keawsawasvong S, Tran DT (2022) Bearing capacity of ring foundations on anisotropic and heterogenous clays: Fea, ngi-adp, and mars. Geotech Geol Eng 40(7):1–16
35. Lashkari A (2010) A SANISAND model with anisotropic elasticity. Soil Dyn Earthq Eng 30(12):1462–477
36. Mašín D, Rott J (2014) Small strain stiffness anisotropy of natural sedimentary clays: review and a model. Acta Geotech 9(2):299–312
37. Mayne PW (1985) Stress anisotropy effects on clay strength. J Geotech Eng 111(3):356–366
38. Mortara G, di Prisco C (2025) On rotational hardening in soil elastic-plasticity. Acta Geotech 20(1):197–210
39. Nakase A, Kamei T (1983) Undrained shear strength anisotropy of normally consolidated cohesive soils. Soils Found 23(1):91–101
40. Ng Ch, Leung E, Lau C (2004) Inherent anisotropic stiffness of weathered geomaterial and its influence on ground deformations around deep excavations. Can Geotech J 41(1):12–24
41. Niemunis A, Grandas-Tavera CE, Prada-Sarmiento LF (2009) Anisotropic visco-hypoplasticity. Acta Geotech 4(4):293–314
42. Niemunis A, Staszewska K (2022) Pure cross-anisotropy for geotechnical elastic potentials. Acta Geotech 17:1699–1717. https://doi.org/10.1007/s11440-021-01284-9
43. Nishimura S, Jardine R.J, Minh N.A (2011) Shear strength anisotropy of natural london clay. In *Stiff sedimentary clays: genesis and engineering behaviour: geótechnique symposium in Print 2007*, Thomas Telford Ltd, pp 97–110
44. Pan K, Cai YQ, Yang ZX, Pan XD (2019) Liquefaction of sand under monotonic and cyclic shear conditions: Impact of drained preloading history. Soil Dyn Earthq Eng 126:105775
45. Petalas A, Dafalias Y, Papadimitriou A (2020) Sanisand-f: Sand constitutive model with evolving fabric anisotropy. Int J Solids Struct 188–189:12–31
46. Petalas A, Dafalias Yannis F, Papadimitriou Achilleas G (2018) Sanisand model simulation under rotation of stress principal axes for granular media. In: *4th international symposium on computational geomechanics*
47. Petalas Alexandros L, Dafalias Yannis F, Papadimitriou Achilleas G (2019) Sanisand-fn: An evolving fabric-based sand model accounting for stress principal axes rotation. Int J Num Anal Methods Geomech 43(1):97–123
48. Piriyakul K, Haegeman W (2009) Stiffness anisotropy of boom clay. In: *17th international conference on soil mechanics and geotechnical engineering*, IOS Press, pp 167–171
49. Atefeh Pirzadeh, Federico Dalla Barba, Florin Bobaru, Lorenzo Sanavia, Mirco Zaccariotto, Ugo Galvanetto (2024) Elastoplastic peridynamic formulation for materials with isotropic and kinematic hardening. Eng Comput 40(4):2063–2082
50. Roscoe KH, Burland JB (1968) On the generalized stress-strain behaviour of "wet" clay. Engineering plasticity. Cambridge University Press, Cambridge, pp 535–609
51. Salehi Ali, Yang Ming, Taiebat Mahdi . Effect of inherent fabric on cyclic resistance of granular materials with static shear: A 3d-dem study. In *Geo-Congress 2024*, pp 120–129
52. Salimi M, Lashkari A, Tafili M (2024) Dem investigation on flow instability of particulate assemblies under coupling between volumetric and axial strains. Acta Geotech 19(11):7261–7286
53. Mohammad Salimi, Merita Tafili, Felipe Prada-Sarmiento Luis, Nazanin Irani, Theodoros Triantafyllidis, Torsten Wichtmann (2025) Dem-cfm analysis of undrained cyclic behavior in transversely isotropic granular soils under true triaxial loading paths. J Geotech Geoenviron Eng 151(5):04025022
54. Salimi Mohammadjavad, Lashkari Ali (2018) Simulation of the undrained behavior of particulate assemblies subjected to continuous rotation of lode angle. In: *proceedings of China-Europe conference on geotechnical engineering, Springer, Vol 1*, pp 61–64
55. Schmidt S, Wiebicke M, Herle I (2022) On the determination and evolution of fabric in representative elementary volumes for a sand specimen in triaxial compression. Granular Matter 24(4):1–9
56. Schropp R (2014) Weitergehende Untersuchungen zum Einfluss der Anisotropie des Tons auf die numerische Prognose des Fließdruckes auf Pfähle. Diploma thesis, Institut für Bodenmechanik und Felsmechanik am Karlsruher Institut für Technologie (KIT)
57. Shi XS, Ivo Herle (2016) Modeling the compression behavior of remolded clay mixtures. Comput Geotech 80:215–225
58. Shogaki T, Kumagai N (2008) A slope stability analysis considering undrained strength anisotropy of natural clay deposits. Soils Found 48(6):805–819
59. Sorensen K, Nielsen V, Mikkelsen A, Stutz HH (2023) Characterization of the rate dependent behavior of a high plasticity stiff sedimentary clay. Geotech Test J 46(6):862–78
60. Tafili M (2020) *Monotonic, cyclic and dilatant behaviour of cohesive soils: constitutive description and experimental observations*. PhD thesis, Veröffentlichungen des Instituts für Bodenmechanik und Felsmechanik am Karlsruher Institut für Technologie (KIT), Vol. 186
61. Tafili M, Duque J, Ochmański M, Mašín D, Wichtmann T (2023) Numerical inspection of miner's rule and drained cyclic preloading effects on fine-grained soils. Comput Geotech 156:105310
62. Tafili M, Ganal A, Wichtmann T, Reul O (2023) On the AVISA model for clay-recommendations for calibration and verification based on the back analysis of a piled raft. Comput Geotech 154:105126
63. Tafili M, Grandas C, Triantafyllidis T, Wichtmann T (2022) Constitutive anamnesis model (CAM) for fine-grained soils. Int J Num Anal Methods Geomech. https://doi.org/10.1002/nag.3428
64. Tafili M, Triantafyllidis Th (2018) On constitutive modelling of anisotropic viscous and non-viscous soft soils. volume 1 of *Numerical Methods in Geotechnical Engineering IX*, Taylor & Francis Group, Porto, Portugal, pp 139–148
65. Tafili M, Triantafyllidis T (2020) AVISA: anisotropic visco-ISA model and its performance at cyclic loading. Acta Geotech 15:2395–24137. https://doi.org/10.1007/s11440-020-00925-9
66. Tafili M, Triantafyllidis T (2020) A simple hypoplastic model with loading surface accounting for viscous and fabric effects of clays. Int J Numer Anal Meth Geomech 44(16):2189–2215
67. Tafili M, Wichtmann T, Triantafyllidis T (2021) Experimental investigation and constitutive modeling of the behaviour of highly plastic lower rhine clay under monotonic and cyclic loading. Can Geotech J 58(9):1396–1410
68. Tafili M (2023) Theodoros Triantafyllidis, and Torsten Wichtmann. Validierung des anisotropen visko isa modells (avisa) für bindige böden. *geotechnik*, 46(1):28–37
69. Toyota H, Nakamura K, Sakai N (2003) Application of the elastic boundary induced by shear history on saturated cohesive soil. Soils Found 43(1):93–100
70. Toyota H, Susami A, Takada S (2014) Anisotropy of undrained shear strength induced by k_0 consolidation and swelling in cohesive soils. Int J Geomech 14(4):04014019
71. Wang L, Shen K, Ye S (2008) Undrained shear strength of k_0 consolidated soft soils. Int J Geomech 8(2):105–113
72. Wichtmann T(2016) Soil behaviour under cyclic loading - experimental observations, constitutive description and applications. Veröffentlichungen des Instituts für Bodenmechanik und Felsmechanik am Karlsruher Institut für Technologie (KIT), Vol 181

73. Wichtmann T, Andersen KH, Sjursen MA (2013) Cyclic behaviour of high-quality undisturbed block samples of Onsøy clay. Canadian Geotech J 50(4):400–412
74. Wichtmann T, Triantafyllidis T (2018) Monotonic and cyclic tests on kaolin: a database for the development, calibration and verification of constitutive models for cohesive soils with focus to cyclic loading. Acta Geotech 13(5):1103–1128
75. Wiebicke M, Andò E, Viggiani G, Herle I (2020) Measuring the evolution of contact fabric in shear bands with x-ray tomography. Acta Geotech 15(1):79–93
76. Yamakawa Y, Hashiguchi K, Sasaki T, Higuchi M, Sato K, Kawai T, Machishima T, Iguchi T (2021) Anisotropic subloading surface cam-clay plasticity model with rotational hardening: Deformation gradient-based formulation for finite strain. Int J Numer Anal Meth Geomech 45(16):2321–2370
77. Soga Yimsiri, Soga K (2010) Dem analysis of soil fabric effects on behaviour of sand. Géotechnique 60(6):483–495
78. Yin Z, Chang Ch, Karstunen M, Hicher P (2010) An anisotropic elastic-viscoplastic model for soft clays. Int J Solids Struct 47(5):665–677